# Pattern of global spin alignment of φ and K\*0 mesons in heavy-ion collisions

https://doi.org/10.1038/s41586-022-05557-5

STAR Collaboration\*

Received: 4 April 2022

Accepted: 11 November 2022

Published online: 18 January 2023



Check for updates

Notwithstanding decades of progress since Yukawa first developed a description of the force between nucleons in terms of meson exchange<sup>1</sup>, a full understanding of the strong interaction remains a considerable challenge in modern science. One remaining difficulty arises from the non-perturbative nature of the strong force, which leads to the phenomenon of quark confinement at distances on the order of the size of the proton. Here we show that, in relativistic heavy-ion collisions, in which quarks and gluons are set free over an extended volume, two species of produced vector (spin-1) mesons, namely φ and K\*0, emerge with a surprising pattern of global spin alignment. In particular, the global spin alignment for  $\phi$  is unexpectedly large, whereas that for K\*0 is consistent with zero. The observed spin-alignment pattern and magnitude for φ cannot be explained by conventional mechanisms, whereas a model with a connection to strong force fields<sup>2-6</sup>, that is, an effective proxy description within the standard model and quantum chromodynamics, accommodates the current data. This connection, if fully established, will open a potential new avenue for studying the behaviour of strong force fields.

At the Relativistic Heavy Ion Collider (RHIC) at Brookhaven National Laboratory, heavy ions (such as gold nuclei) are accelerated up to 99.995% of the speed of light and collide from opposite directions. Owing to the extreme conditions achieved, quarks and gluons are liberated for a brief time (about 10<sup>-23</sup> s), instead of being confined inside particles such as protons and neutrons by the strong force. The hot and dense state of matter formed in these collisions is called the quarkgluon plasma (QGP)<sup>7-10</sup>. These collisions offer an ideal environment for studying phenomena related to quantum chromodynamics, the theory of strong interaction among quarks and gluons.

In collisions that are not exactly head-on, the approach paths of the two nuclei are displaced by a distance called the impact parameter (b). generating a very large orbital angular momentum (OAM) in the system. Part of the OAM is transferred to the QGP in the form of fluid vorticity along the OAM direction, which can polarize the spin of the particles through spin-orbit coupling, a phenomenon called global polariza $tion {}^{11-16}. According to the flavour-spin wave function, the polarization \\$ of the  $\Lambda(\overline{\Lambda})$  hyperon is carried solely by the strange quark s  $(\overline{s})$ , indicating the global polarization of the s  $(\bar{s})$  quark<sup>17</sup>. The global polarization of  $\Lambda(\overline{\Lambda})$  hyperons produced in heavy-ion collisions has been studied through their decays by the STAR<sup>18-20</sup>, the ALICE<sup>21</sup> and the HADES<sup>22</sup>

The global polarization of quarks influences production of vector mesons such as  $\phi(1020)$  and  $K^{*0}(892)$ . Unlike  $\Lambda(\overline{\Lambda})$  hyperons, which can undergo weak decay with parity violation, and for which the products in the rest frame of the decay are emitted preferentially in the spin direction, the polarization of vector mesons cannot be directly measured because they mainly decay through the strong interaction, in which parity is conserved. Nevertheless, the spin state of a vector meson can be described by a  $3 \times 3$  spin density matrix with unit trace<sup>23</sup>. The diagonal elements of this matrix, namely  $\rho_{11}$ ,  $\rho_{00}$  and  $\rho_{-1-1}$ , are probabilities for the spin component along a quantization axis to take the values of 1, 0 and -1, respectively. The quantization axis is a chosen axis onto which the projection of angular momentum has well-defined quantum numbers. When the three spin states have equal probability to be occupied, all three elements are 1/3 and there is no spin alignment. If  $\rho_{00} \neq 1/3$ , the probabilities of the three spin states along the quantization axis are different and there is a spin alignment. In the rest frame of a vector meson decaying to two particles, the angular distribution of one of the decay products can be written as

$$\frac{dN}{d(\cos\theta^*)} \propto (1 - \rho_{00}) + (3\rho_{00} - 1)\cos^2\theta^*,\tag{1}$$

in which  $\theta^*$  is the polar angle between the quantization axis and the momentum direction of that decay particle. By fitting the angular distribution of decay particles with the function above, one can infer the  $\rho_{00}$  value. For the study of global spin alignment, the quantization axis  $(\hat{n})$  is chosen to be the direction of the OAM  $(\hat{L})$ , which is perpendicular to the reaction plane. The reaction plane is defined by the direction of the colliding nuclei (beam direction) and the impact parameter vector  $(\hat{b})^{24}$ . See Fig. 1 for a schematic view of the coordinate setup for measuring global spin alignment in heavy-ion collisions. φ mesons are identi fied by means of their decay  $\phi \to K^+ + K^-$ . The  $\underline{K}^{*0}$  and  $\overline{K}^{*0}$  mesons are reconstructed by means of their decay  $K^{*0}$  ( $\overline{K}^{*0}$ )  $\to K^+\pi^-$  ( $K^-\pi^+$ ). Hereafter,  $K^{*0}$  refers to the combination of  $K^{*0}$  and  $\overline{K^{*0}}$  unless otherwise

It is assumed  $^{2,12,25-27}$  that the global spin alignment of  $\varphi$  mesons can be produced by the coalescence of polarized s and \$\overline{s}\$ quarks, which can be caused by vortical flow or the local fluctuation of mean field (meson field). The conventional sources for the polarization of s and \(\bar{s}\) quarks include: the vortical flow  $^{25,28}$  in the QGP in collisions with non-zero

<sup>\*</sup>A list of authors and their affiliations appears at the end of the paper.

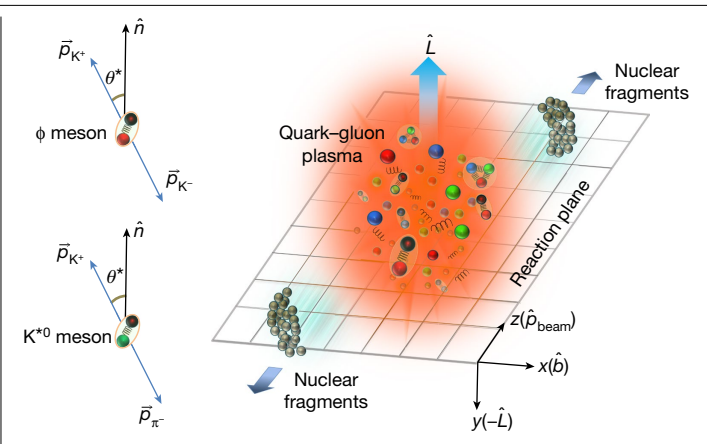


Fig. 1 | A schematic view of the coordinate setup for measuring global spin alignment in heavy-ion collisions. Two nuclei collide and a tiny exploding QGP fireball, only a few femtometres across, is formed in the middle. The direction of the orbital angular momentum  $(\hat{L})$  is perpendicular to the reaction plane defined by the incoming nuclei when  $b \neq 0$ . The symbol  $\vec{p}$  represents the momentum vector of a particle. At the top-left corner, a φ meson, composed of s and  $\bar{s}$  quarks, is depicted separately as a particle decaying into a  $(K^+, K^-)$  pair. In this example, the quantization axis  $(\hat{n})$  for study of the global spin alignment of the  $\phi$  meson is set to be the same as  $\hat{L}$ .  $\theta^*$  is the polar angle between the quantization axis and the momentum direction of a particle in the rest frame of the decay. A similar depiction can be found for a K\*0 meson at the bottom-left corner.

impact parameter, the electromagnetic fields<sup>2,25</sup> generated by the electric currents carried by the colliding nuclei, quark polarization along the direction of its momentum (helicity polarization)<sup>27</sup> and the spin alignment produced by fragmentation of polarized quarks<sup>12</sup>. Both the vorticity and electromagnetic fields can be represented as relativistic, rank-2 tensors having 'electric' (space-time) and 'magnetic' (space-space) components; each contributes to the quark polarization along the quantization axis  $\hat{n}$ . For the  $\Lambda$  and  $\overline{\Lambda}$  polarization in the rest frame, the only contribution is from the magnetic components, in which the vorticity contribution dominates. STAR measurements of the polarization of  $\Lambda$  and  $\overline{\Lambda}$  (refs. <sup>18,19</sup>) indicate that the magnetic components of the vorticity and the electromagnetic field tensor in total give<sup>2,12,25</sup> a negative contribution to  $\rho_{00}$  at the level of  $10^{-5}$ . Furthermore, the local vorticity loop in the transverse plane26, when acting together with coalescence, gives a negative contribution to global  $ho_{00}$ . From a hydrodynamic simulation of the vorticity field in heavy-ion collisions, it is known<sup>2</sup> that the electric component of the vorticity tensor gives a contribution on the order of 10<sup>-4</sup>. Simulation of the electromagnetic field in heavy-ion collisions indicates<sup>2</sup> that the electric field gives a contribution on the order of 10<sup>-5</sup>. Fragmentation of polarized quarks contributes on the order of 10<sup>-5</sup> and the effect is mainly present in transverse momenta much larger than a few GeV  $c^{-1}$  (ref.  $^{12}$ ). Helicity polarization gives a negative contribution at all centralities<sup>27</sup>. Locally fluctuating axial charge currents induced by possible local charge violation gives rise to the expectation<sup>29</sup> of  $\rho_{00}(K^{*0}) < \rho_{00}(\Phi) < 1/3$ . The aforementioned mostly conventional mechanisms make either positive or negative contributions to  $\phi$ -meson  $\rho_{00}$ , but none of them can produce a  $\rho_{00}$  that is larger than 1/3 by more than a few times  $10^{-4}$ . Recently, a theoretical model was proposed on the basis of the φ-meson vector field coupling to s and  $\bar{s}$  quarks<sup>2-6</sup>, analogous to the photon vector field coupled to electrically charged particles. In this mechanism, the observed global spin alignment is caused by the local fluctuation of the strong force field and can cause deviations of  $\rho_{00}$  from 1/3 larger than 10<sup>-4</sup>.

 $In 2008, the \, STAR \, Collaboration \, reported \, on \, a \, search \, for \, global \, spin$ alignment of  $\phi(1020)$  and  $K^{*0}(892)$  mesons for Au+Au collisions at a centre-of-mass energy per nucleon pair of  $\sqrt{s_{\rm NN}}$  = 200 GeV , with  $\hat{n}$ 

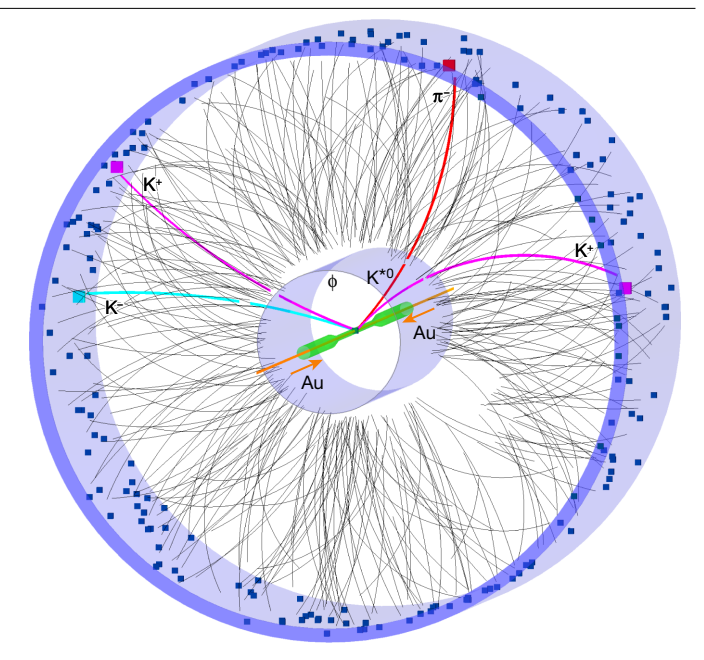
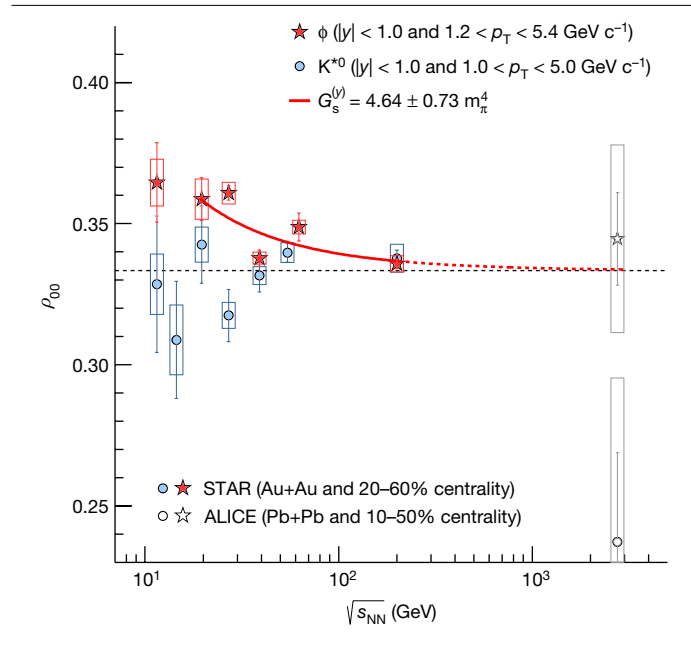


Fig. 2 | Schematic display of a single Au+Au collision at  $\sqrt{s_{NN}}$  = 27 GeV in the **STAR detector.** A three-dimensional rendering of the STAR TPC, surrounded by the TOF barrel shown as the outermost cylinder. The beam pipe is shown in green and, inside it, gold ions travel in opposite directions along the beam axis (brown). Ions collide at the centre of the TPC and trajectories (grey lines) as well as TOF hits (blue squares) from a typical collision are shown. Reconstructed trajectories of a (K<sup>+</sup>, K<sup>-</sup>) pair originating from a φ-meson decay, as well as a K<sup>+</sup> and  $\pi^-$  from a K\*0-meson decay, are shown as highlighted tracks.

oriented along  $\hat{L}$  (ref. <sup>30</sup>). Owing to limited statistics at that time, no notable result was reported. In the present paper, we report the STAR Collaboration's measurement of spin alignment for φ and K\*0 vector mesons with much larger statistics and at lower collision energies.

The relevant features of the STAR experiment used for the spin alignment measurements are depicted in Fig. 2. The two charged daughter particles leave ionization trails inside the STAR Time Projection Chamber (TPC)<sup>31</sup>, with trajectories bent in the magnetic field, by which momentum information for charged particles can be reconstructed and the ionization energy loss (dE/dx) inside the gas of the TPC can be calculated. Furthermore, the time-of-flight information for particles can be obtained from the STAR Time-of-Flight (TOF) detector<sup>32</sup> and, combining this with dE/dx measurements, the momentum and particle species  $for daughters \, can \, be \, determined. \, Figure \, 2 \, shows \, a \, three-dimensional \, a \, determined \, a \,$ view of φ and K\*0 mesons decaying into their corresponding daughters inside the TPC. More details on the measurement procedure can be found in Methods.

Figure 3 shows  $\rho_{00}$  for  $\Phi$  and  $K^{*0}$  for Au+Au collisions at beam energies between  $\sqrt{s_{NN}}$  = 11.5 and 200 GeV. The centrality categorizes events on the basis of the observed multiplicity of produced charge hadrons emitted from each collision, in which 0% centrality corresponds to exactly head-on collisions, which produce the highest multiplicity, whereas 100% centrality corresponds to barely glancing collisions, which produce the lowest multiplicity. The STAR measurements presented in Fig. 3 are for centralities between 20% and 60%. The quantization axis  $(\hat{n})$  is taken to be the normal to the second-order event plane<sup>24</sup> determined using TPC tracks. The second-order event plane, with its orientation corresponding to the elliptic flow of produced hadrons, serves as a proxy for the reaction plane. The φ-meson results are presented for  $1.2 < p_T < 5.4 \text{ GeV } c^{-1}$  and  $|y| < 1.0 \cdot p_T$  is the momentum in the plane transverse to the beam axis and rapidity  $y = \tanh^{-1} \beta_z$ , with  $\beta_z$  being the component of velocity along the beam direction in units of the speed of light.  $\rho_{00}$  for the  $\phi$  meson is much greater than 1/3 for



**Fig. 3** | **Global spin alignment of φ and K\*0 vector mesons in heavy-ion collisions.** The measured matrix element  $\rho_{00}$  as a function of beam energy for the φ and K\*0 vector mesons within the indicated windows of centrality, transverse momentum ( $\rho_{\rm T}$ ) and rapidity (y). The open symbols indicate ALICE results³3 for Pb+Pb collisions at 2.76 TeV at  $\rho_{\rm T}$  values of 2.0 and 1.4 GeV c<sup>-1</sup> for the φ and K\*0 mesons, respectively, corresponding to the  $\rho_{\rm T}$  bin nearest to the mean  $\rho_{\rm T}$  for the 1.0–5.0 GeV c<sup>-1</sup> range assumed for each meson in the present analysis. The solid red curve is a fit to data in the range  $\sqrt{s_{\rm NN}} = 19.6 - 200$  GeV, based on a theoretical calculation with a φ-meson field². Parameter sensitivity of  $\rho_{00}$  to the φ-meson field is shown in ref. <sup>5</sup>. The dashed red line is an extension of the solid curve with the fitted parameter  $G_{\rm S}^{(0)}$ . The dashed black line represents  $\rho_{00} = 1/3$ .

collision energies of 62 GeV and below, indicating finite global spin alignment. The  $\rho_{00}$  for  $\varphi$  mesons, averaged over beam energies between 11.5 and 62 GeV, is 0.3512  $\pm$  0.0017 (stat.)  $\pm$  0.0017 (syst.). Taking the total uncertainty as the sum in quadrature of statistical and systematic uncertainties, our results indicate that the  $\varphi$ -meson  $\rho_{00}$  is above 1/3 with a significance of 7.4  $\sigma$ .

The  $\rho_{00}$  for K\*0 is shown for 1.0 <  $p_{\rm T}$  < 5.0 GeV c $^{-1}$ . We observe that  $\rho_{00}$  for K\*0 is consistent with 1/3, in marked contrast to the results for  $\varphi$ . The  $\rho_{00}$  for K\*0, averaged over beam energies of 54.4 GeV and below, is 0.3356  $\pm$  0.0034 (stat.)  $\pm$  0.0043 (syst.). The complete set of results for  $p_{\rm T}$  and centrality dependence for both vector mesons can be found in Methods. Measurements from the ALICE Collaboration for Pb+Pb collisions at  $\sqrt{s_{\rm NN}}=2.76$  TeV (ref.  $^{33}$ ), taken from the closest data points  $^{33}$  to the mean  $p_{\rm T}$  for the range 1.0 <  $p_{\rm T}$  < 5.0 GeV c $^{-1}$ , are also shown for comparison in Fig. 3.

Intriguingly,  $p_{\text{T}}$ -averaged  $\phi$ -meson data at intermediate centrality can be explained by the theoretical model invoking the  $\phi$ -meson vector field<sup>2-6</sup>. This can be seen by fitting the data, as presented by the solid red curve in Fig. 3. This model fit involves adjusting  $G_s^{(y)}$ , which represents³ the quadratic form of field strength tensors multiplied by the effective coupling constant  $(g_{\phi})$ . In its specific form,  $G_s^{(y)} \equiv g_{\phi}^2 \left[ 3\langle B_{\phi,y}^2 \rangle + \frac{\langle \mathbf{p}^2 \rangle_{\phi}}{m_s^2} \langle E_{\phi,y}^2 \rangle - \frac{3}{2}\langle B_{\phi,x}^2 + B_{\phi,z}^2 \rangle - \frac{\langle \mathbf{p}^2 \rangle_{\phi}}{2m_s^2} \langle E_{\phi,x}^2 + E_{\phi,z}^2 \rangle \right]$ ,

in which  $E_{\Phi,i}$  and  $B_{\Phi,i}$  are the ith component of the analogous electric and magnetic parts of the  $\phi$ -meson field, respectively, and  $m_s$  is the s-quark mass and  $\mathbf{p}$  its momentum in the  $\phi$  rest frame. The stronger deviation of  $\rho_{00}$  from 1/3 observed at lower energy is explained by  $1/T_{\rm eff}^2$  dependence originating in the theoretical description from the polarization of quarks in the  $\phi$ -meson field. Here  $T_{\rm eff}$  is the effective temperature of the QGP fireball. This model can accommodate the large

magnitude of  $\rho_{00}$  as seen in our measurement and it also gives the correct collision-energy dependence. The  $p_{\rm T}$  and centrality dependence of the large  $\rho_{00}$  signal is recently described by an improved version of the model, which is derived from the relativistic spin Boltzmann equation<sup>5</sup>.

The relationship of the  $\phi$  meson to the  $\phi$ -meson field is similar to that of the photon to the electromagnetic field. In analogy to the way in which the photon mediates the electromagnetic interaction, the Φ meson can be considered a mediator of the nuclear interaction. The Φ-meson field behaves like the electromagnetic field because both are vector fields, but the  $\Phi$ -meson field is one component of the short-distance (a few femtometres) strong force, whereas the electromagnetic field is a long-distance force. The φ-meson fields, along with other meson fields such as  $\sigma$ ,  $\pi$ ,  $\rho$ ,  $\omega$  and so on, are low-energy or intermediate-distance (on the order of nuclear radii) effective modes of  $q\bar{q}$  (refs. <sup>34,35</sup>). These modes with the vacuum quantum number are in connection with modes of two gluon fields in quantum chromodynamics<sup>36</sup>. Just as an electric charge in motion can generate an electromagnetic field, the strange quarks s and  $\bar{s}$  in motion can produce an effective  $\phi$ -meson field. The local difference between the currents of s and s (net-strangeness current), which may occur because the s and s have different momenta at a given space-time point, can generate an effective φ-meson field. Through its magnetic part, the vector meson field has been used to predict the difference between the polarization of  $\Lambda$  and  $\overline{\Lambda}$  (ref. <sup>37</sup>). Similar to how an electric field can polarize a quark and antiquark through spin-orbit couplings, the strong electric part of the  $\phi$ -meson field can also polarize s and  $\bar{s}$ , leading to a positive contribution to  $\rho_{00}$  of the  $\phi$  meson (as a bound state of s and  $\bar{s}$ ) but with much larger magnitude owing to its strong interaction (a large coupling constant  $g_{\phi}$ ). Figure 3 shows that, although conventional explanations fall far short in accounting for the data, our experimental measurement in 20-60% centrality can be described well by this model, which invokes the  $\varphi\text{-meson}$  field, thus favouring the conclusion that the  $\varphi\text{-meson}$ field leads to the  $\phi$ -meson global spin alignment.

The lifetime of  $K^{*0}$  is about ten times shorter than the  $\phi$  lifetime, corresponding to a mean proper decay length  $c\tau \approx 4.1$  fm, making it susceptible to in-medium effects. The difference between the global spin alignment for  $K^{*0}$  and  $\Phi$  may be attributed to different in-medium interactions resulting from this difference in lifetime, a polarization transfer during the late stage of hadronic interactions<sup>38</sup> and a different response to the vector meson field<sup>2</sup>. Similar to strange quarks (s and  $\bar{s}$ ), light quarks can also be polarized by vorticity fields and vector meson fields. However, the vector fields that polarize light quarks, such as the  $\rho$  and  $\omega$  fields, are distinct from the  $\phi$  field that polarizes strange quarks. The contributions from vector meson fields to  $\rho_{00}$  for K<sup>\*0</sup> involve averages of products of different vector meson fields, such as that from the  $\phi$  (for the  $\bar{s}$ ) and  $\rho$  (for the d). It is expected that the correlations between these two different, fluctuating vector meson fields for d and s are much weaker than the correlations between the same fields for s and  $\bar{s}$ , causing the vector meson field contributions to  $\rho_{00}$  for K\*0 to be negligible<sup>4</sup>. The above considerations may account for the small deviation of  $\rho_{00}$  for K\*0 from 1/3, as observed in experiments. A comprehensive and quantitative study of all these effects is needed to show the nature of such a marked difference between spin alignments of K\*0 and φ. Our new data provide motivation for further theoretical developments in this direction.

On the basis of the fit to our data in Fig. 3 with the model in ref.  $^2$ , we estimate the free parameter in the fit,  $G_s^{(y)}$ , to be  $4.64\pm0.73m_\pi^4$ . This value of  $G_s^{(y)}$  is compatible with the value of the average field squared times  $g_{\Phi}^2$  used in the calculation of the relativistic spin Boltzmann equation 5. The extracted value serves as only a rough estimate, as uncertainties and assumptions in ref.  $^2$  await further studies by the theoretical community. This is a qualitatively new class of measurement and it offers important guidance for future theoretical progress concerning the strong force field under extreme conditions.

Measurements of the global spin alignment of vector mesons provide new knowledge about the vector meson fields. The vector meson fields are an essential part of the nuclear force that binds nucleons inside atomic nuclei<sup>39,40</sup> and are also pivotal in describing properties of nuclear structure and nuclear matter  $^{34,41}$ . The  $ho_{00}$  for the  $\phi$  meson has a desirable feature in that all contributions depend on squares of field amplitudes; it can be considered a field analyser<sup>2</sup>, which makes it possible to extract the imprint of the  $\varphi\text{-meson}$  field even if the field fluctuates strongly in space-time. Another important feature worthy of mention is that an essential contribution to the  $\Phi$ -meson  $\rho_{00}$  is from the term<sup>2</sup>  $\approx$  **S** · ( $\mathbf{E}_{\Phi} \times \mathbf{p}$ ), in which  $\mathbf{E}_{\Phi}$  is the electric part of the  $\Phi$ -meson field induced by the local, net strangeness current density, and S and p are the spin and momentum of the strange (anti) quarks, respectively. Such a term is nothing but the quark version of the spin-orbit force. which-at the nucleon level-plays a key role in the nuclear shell structure 42,43. Our measurements of a signal based on global spin alignment for vector mesons show a surprising pattern and a value for the φ meson that is orders of magnitude larger than can be explained by conventional effects. This work provides a potential new avenue for understanding the strong interaction at work at the subnucleon level.

#### **Online content**

Any methods, additional references, Nature Portfolio reporting summaries, source data, extended data, supplementary information, acknowledgements, peer review information; details of author contributions and competing interests; and statements of data and code availability are available at https://doi.org/10.1038/s41586-022-05557-5.

- 1. Yukawa, H. On the interaction of elementary particles. I. Proc. Phys. Math. Soc. Jpn. 17,
- Sheng, X.-L., Oliva, L. & Wang, Q. What can we learn from the global spin alignment of  $\phi$ mesons in heavy-ion collisions? Phys. Rev. D 101, 096005 (2020).
- Sheng, X.-L., Oliva, L. & Wang, Q. Erratum: What can we learn from the global spin alignment of  $\phi$  mesons in heavy-ion collisions? Phys. Rev. D 105, 099903 (2022).
- Sheng, X.-L., Wang, Q. & Wang, X.-N. Improved guark coalescence model for spin alignment and polarization of hadrons. Phys. Rev. D 102, 056013 (2020)
- Sheng, X.-L., Oliva, L., Liang, Z.-T., Wang, Q. & Wang, X.-N. Spin alignment of vector mesons in heavy-ion collisions. Preprint at https://arxiv.org/abs/2205.15689 (2022).
- 6 Sheng, X.-L., Oliva, L., Liang, Z.-T., Wang, Q. & Wang, X.-N. Relativistic spin dynamics for vector mesons. Preprint at https://arxiv.org/abs/2206.05868 (2022).
- Arsene, I. et al. Quark-gluon plasma and color glass condensate at RHIC? The perspective from the BRAHMS experiment. Nucl. Phys. A 757, 1-27 (2005).
- 8. Back, B. B. et al. The PHOBOS perspective on discoveries at RHIC. Nucl. Phys. A 757, 28-101 (2005)
- Adams, J. et al. Experimental and theoretical challenges in the search for the quark-gluon plasma: the STAR Collaboration's critical assessment of the evidence from RHIC collisions. Nucl. Phys. A 757, 102-183 (2005).
- Adcox, K. et al. Formation of dense partonic matter in relativistic nucleus-nucleus collisions at RHIC: experimental evaluation by the PHENIX Collaboration. Nucl. Phys. A **757**, 184-283 (2005).
- Liang, Z.-T. & Wang, X.-N. Globally polarized quark-gluon plasma in noncentral A+A collisions. Phys. Rev. Lett. 94, 102301 (2005); erratum: 96, 039901(2006).
- Liang, Z.-T. & Wang, X.-N. Spin alignment of vector mesons in non-central A + A collisions. Phys. Lett. B 629, 20-26 (2005).
- Voloshin, S. A. Polarized secondary particles in unpolarized high energy hadron-hadron collisions? Preprint at https://arxiv.org/abs/nucl-th/0410089 (2004).
- Betz, B., Gyulassy, M. & Torrieri, G. Polarization probes of vorticity in heavy ion collisions. Phys. Rev. C 76, 044901 (2007).
- 15. Becattini, F., Piccinini, F. & Rizzo, J. Angular momentum conservation in heavy ion collisions at very high energy. Phys. Rev. C 77, 024906 (2008).
- Gao, J.-H. et al. Global quark polarization in noncentral A + A collisions. Phys. Rev. C 77, 044902 (2008).
- Close, F. E. An Introduction to Quarks and Partons (Academic, 1979)
- Adamczyk, L, et al. Global Λ hyperon polarization in nuclear collisions: evidence for the most vortical fluid. Nature 548, 62-65 (2017).
- 19. Adam, J. et al. Global polarization of  $\Lambda$  hyperons in Au + Au collisions at  $\sqrt{s_{NM}}$  = 200 GeV. Phys. Rev. C 98, 014910 (2018).
- 20. Abdallah, M. S. et al. Global  $\Lambda$ -hyperon polarization in Au + Au collisions at  $\sqrt{s_{NN}}$  = 3 GeV. Phys. Rev. C 104, L061901 (2021).
- Acharya, S. et al. Global polarization of  $\Lambda$  and  $\overline{\Lambda}$  hyperons in Pb-Pb collisions at  $\sqrt{s_{NN}}$  = 2.76 and 5.02 TeV. Phys. Rev. C 101, 044611 (2020).
- Kornas, F. J. Systematics in the global polarization measurements of  $\Lambda$  hyperons with HADES at SIS18. EPJ Web Conf. 259, 11016 (2022).
- Schilling, K., Seyboth, P. & Wolf, G. E. On the analysis of vector-meson production by polarized photons. Nucl. Phys. B 15, 397-412 (1970); erratum 18, 332 (1970).

- Poskanzer, A. M. & Voloshin, S. A. Methods for analyzing anisotropic flow in relativistic nuclear collisions. Phys. Rev. C 58, 1671-1678 (1998).
- Yang, Y.-G., Fang, R.-H., Wang, Q. & Wang, X.-N. Quark coalescence model for polarized vector mesons and baryons. Phys. Rev. C 97, 034917 (2018).
- Xia, X.-L., Li, H., Huang, X.-G. & Zhong Huang, H. Local spin alignment of vector mesons in relativistic heavy-ion collisions. Phys. Lett. B 817, 136325 (2021).
- Gao, J.-H. Helicity polarization in relativistic heavy ion collisions. Phys. Rev. D 104, 076016
- 28. Becattini, F., Csernai, L. & Wang, D. J. A polarization in peripheral heavy ion collisions. Phys. Rev. C 88, 034905 (2013); erratum 93, 069901 (2016).
- Müller, B. & Yang, D.-L. Anomalous spin polarization from turbulent color fields. Phys. Rev. D 105 | D11901 (2022)
- Abelev, B. I. et al. Spin alignment measurements of the  $K^{*0}(892)$  and  $\phi(1020)$  vector mesons in heavy ion collisions at  $\sqrt{s_{NN}}$  = 200 GeV. Phys. Rev. C 77, 061902 (2008).
- Anderson, M. et al. The STAR time projection chamber: a unique tool for studying high multiplicity events at RHIC. Nucl. Instrum. Methods Phys. Res. A 499, 659-678 (2003).
- 32. Llope, W. J. Multigap RPCs in the STAR experiment at RHIC. Nucl. Instrum. Methods Phys. Res. A 661, S110-S113 (2012).
- Acharva, S. et al. Evidence of spin-orbital angular momentum interactions in relativistic heavy-ion collisions, Phys. Rev. Lett. 125, 012301 (2020).
- Serot, B. D. & Walecka, J. D. The relativistic nuclear many body problem, Adv. Nucl. Phys. 16, 1-327 (1986).
- Gasser, J. & Leutwyler, H. Chiral perturbation theory to one loop. Ann. Phys. 158, 142–210 (1984)
- 36. Shifman, M. A., Vainshtein, A. I. & Zakharov, V. I. Remarks on Higgs-boson interactions with nucleons. Phys. Lett. B 78, 443-446 (1978).
- Csernai, L. P., Kapusta, J. I. & Welle, T.  $\Lambda$  and  $\overline{\Lambda}$  spin interaction with meson fields generated by the baryon current in high energy nuclear collisions. Phys. Rev. C 99, 021901 (2019).
- Karpenko, I. & Becattini, F. Study of Λ polarization in relativistic nuclear collisions at 38 s<sub>NN</sub> 7.7–200 GeV. Eur. Phys. J. C **77**, 213 (2017).
- Bryan, R. & Scott, B. L. Nucleon-nucleon scattering from one-boson-exchange potentials. III. S waves included. Phys. Rev. 177, 1435-1442 (1969)
- Nagels, M. M., Rijken, T. A. & de Swart, J. J. Low-energy nucleon-nucleon potential from Regge-pole theory. Phys. Rev. D 17, 768 (1978).
- Walecka, J. D. A theory of highly condensed matter. Ann. Phys. 83, 491-529 (1974).
- Mayer, M. G. On closed shells in nuclei. II. Phys. Rev. 75, 1969-1970 (1949).
- Haxel, O., Jensen, J. H. D. & Suess, H. E. On the "magic numbers" in nuclear structure. Phys. Rev. 75, 1766 (1949).

Publisher's note Springer Nature remains neutral with regard to jurisdictional claims in published maps and institutional affiliations.

Springer Nature or its licensor (e.g. a society or other partner) holds exclusive rights to this article under a publishing agreement with the author(s) or other rightsholder(s); author self-archiving of the accepted manuscript version of this article is solely governed by the terms of such publishing agreement and applicable law.

© The Author(s), under exclusive licence to Springer Nature Limited 2023

#### STAR Collaboration<sup>™</sup>

M. S. Abdallah<sup>1</sup>, B. E. Aboona<sup>2</sup>, J. Adam<sup>3</sup>, L. Adamczyk<sup>4</sup>, J. R. Adams<sup>5</sup>, J. K. Adkins<sup>6</sup>, G. Agakishiev<sup>7</sup>, I. Aggarwal<sup>8</sup>, M. M. Aggarwal<sup>8</sup>, Z. Ahammed<sup>9</sup>, A. Aitbaev<sup>7</sup>, I. Aleksee D. M. Anderson<sup>2</sup>, A. Aparin<sup>7</sup>, E. C. Aschenauer<sup>3</sup>, M. U. Ashraf<sup>12</sup>, F. G. Atetalla<sup>13</sup>, G. S. Averichev<sup>7</sup>, V. Bairathi<sup>14</sup>, W. Baker<sup>15</sup>, J. G. Ball Cap<sup>16</sup>, K. Barish<sup>15</sup>, A. Behera<sup>17</sup> R. Bellwied<sup>16</sup>, P. Bhagat<sup>18</sup>, A. Bhasin<sup>18</sup>, J. Bielcik<sup>19</sup>, J. Bielcikova<sup>20</sup>, I. G. Bordyuzhin<sup>10</sup>, J. D. Brandenburg<sup>3</sup>, A. V. Brandin<sup>11</sup>, X. Z. Cai<sup>21</sup>, H. Caines<sup>22</sup>, M. Calderón de la Barca Sánchez<sup>23</sup>, D. Cebra<sup>23</sup>, I. Chakaberia<sup>24</sup>, P. Chaloupka<sup>19</sup>, B. K. Chan<sup>25</sup>, F.-H. Chang<sup>26</sup>, Z. Chang<sup>3</sup>, A. Chatterjee<sup>27</sup>, S. Chattopadhyay<sup>9</sup>, D. Chen<sup>15</sup>, J. Chen<sup>28</sup>, J. H. Chen<sup>29</sup>, X. Chen<sup>30</sup>, Z. Chen<sup>28</sup>, J. Cheng<sup>31</sup>, S. Choudhury<sup>29</sup>, W. Christie<sup>3</sup>, X. Chu<sup>3</sup>, H. J. Crawford<sup>32</sup>, M. Csanád<sup>33</sup> M. Daugherity<sup>34</sup>, T. G. Dedovich<sup>7</sup>, I. M. Deppner<sup>35</sup>, A. A. Derevschikov<sup>36</sup>, A. Dhamija<sup>8</sup>, L. Di Carlo<sup>37</sup>, L. Didenko<sup>3</sup>, P. Dixit<sup>38</sup>, X. Dong<sup>24</sup>, J. L. Drachenberg<sup>34</sup>, E. Duckworth<sup>13</sup> J. C. Dunlop<sup>3</sup>, J. Engelage<sup>32</sup>, G. Eppley<sup>39</sup>, S. Esumi<sup>40</sup>, O. Evdokimov<sup>41</sup>, A. Ewigleben<sup>42</sup>, O. Eyser<sup>3</sup>, R. Fatemi<sup>6</sup>, F. M. Fawzi<sup>1</sup>, S. Fazio<sup>43</sup>, C. J. Feng<sup>26</sup>, Y. Feng<sup>44</sup>, E. Finch<sup>45</sup>, Y. Fisyak<sup>3</sup>, A. Francisco<sup>22</sup>, C. Fu<sup>12</sup>, C. A. Gagliardi<sup>2</sup>, T. Galatyuk<sup>46</sup>, F. Geurts<sup>39</sup>, N. Ghimire<sup>47</sup>, A. Gibson<sup>48</sup>, K. Gopal<sup>49</sup>, X. Gou<sup>28</sup>, D. Grosnick<sup>48</sup>, A. Gupta<sup>18</sup>, W. Guryn<sup>3</sup>, A. Hamed<sup>1</sup>, Y. Han<sup>3</sup> S. Harabasz<sup>46</sup>, M. D. Harasty<sup>23</sup>, J. W. Harris<sup>22</sup>, H. Harrison<sup>6</sup>, S. He<sup>12</sup>, W. He<sup>29</sup>, X. H. He<sup>50</sup>, Y. He<sup>28</sup>, S. Heppelmann<sup>23</sup>, N. Herrmann<sup>35</sup>, E. Hoffman<sup>16</sup>, L. Holub<sup>19</sup>, C. Hu<sup>50</sup>, Q. Hu<sup>50</sup>, Y. Hu<sup>29</sup> H. Huang<sup>26</sup>, H. Z. Huang<sup>25</sup>, S. L. Huang<sup>77</sup>, T. Huang<sup>26</sup>, X. Huang<sup>31</sup>, Y. Huang<sup>31</sup>, T. J. Humanic<sup>5</sup>, D. Isenhower<sup>34</sup>, M. Isshiki<sup>40</sup>, W. W. Jacobs<sup>51</sup>, C. Jena<sup>49</sup>, A. Jentsch<sup>3</sup>, Y. Ji<sup>24</sup>, J. Jia<sup>317</sup>, K. Jiang<sup>31</sup> X. Ju<sup>30</sup>, E. G. Judd<sup>32</sup>, S. Kabana<sup>14</sup>, M. L. Kabir<sup>15</sup>, S. Kagamaster<sup>42</sup>, D. Kalinkin<sup>3,15</sup>, K. Kang<sup>31</sup> D. Kapukchyan<sup>15</sup>, K. Kauder<sup>3</sup>, H. W. Ke<sup>3</sup>, D. Keane<sup>13</sup>, A. Kechechyan<sup>7</sup>, M. Kelsey<sup>37</sup>, D. P. Kikoła<sup>27</sup>, B. Kimelman<sup>23</sup>, D. Kincses<sup>33</sup>, I. Kisel<sup>52</sup>, A. Kiselev<sup>3</sup>, A. G. Knospe<sup>42</sup>, H. S. Ko<sup>24</sup>, L. Kochenda<sup>11</sup>, A. Korobitsin<sup>7</sup>, L. K. Kosarzewski<sup>19</sup>, L. Kramarik<sup>19</sup>, P. Kravtsov<sup>11</sup>, L. Kumar<sup>8</sup>, S. Kumar<sup>5</sup> R. Eunnawalkam Elayavalli<sup>22</sup>, J. H. Kwasizur<sup>51</sup>, R. Lacey<sup>17</sup>, S. Lan<sup>12</sup>, J. M. Landgraf<sup>3</sup>, J. Lauret<sup>3</sup>, A. Lebedev<sup>3</sup>, R. Lednicky<sup>7</sup>, J. H. Lee<sup>3</sup>, Y. H. Leung<sup>24</sup>, N. Lewis<sup>3</sup>, C. Li<sup>28</sup>, C. Li<sup>30</sup>, W. Li<sup>39</sup>, X. Li<sup>30</sup>, Y. Li<sup>31</sup>, X. Liang<sup>15</sup>, Y. Liang<sup>13</sup>, R. Licenik<sup>20</sup>, T. Lin<sup>28</sup>, Y. Lin<sup>12</sup>, M. A. Lisa<sup>5</sup>, F. Liu<sup>12</sup>, H. Liu<sup>51</sup>, H. Liu<sup>12</sup>, P. Liu<sup>17</sup>, T. Liu<sup>22</sup>, X. Liu<sup>5</sup>, Y. Liu<sup>2</sup>, Z. Liu<sup>30</sup>, T. Ljubicic<sup>3</sup>, W. J. Llope<sup>37</sup>, R. S. Longacre<sup>3</sup>, E. Loyd<sup>15</sup> T. Lu<sup>50</sup>, N. S. Lukow<sup>47</sup>, X. F. Luo<sup>12</sup>, L. Ma<sup>29</sup>, R. Ma<sup>3</sup>, Y. G. Ma<sup>29</sup>, N. Magdy<sup>41</sup>, D. Mallick<sup>5</sup> S. L. Manukhov7, S. Margetis13, C. Markert54, H. S. Matis24, J. A. Mazer55, N. G. Minaev36, S. Mioduszewski<sup>2</sup>, B. Mohanty<sup>53</sup>, M. M. Mondal<sup>17</sup>, I. Mooney<sup>37</sup>, D. A. Morozov<sup>36</sup> A. Mukherjee<sup>33</sup>, M. Nagy<sup>33</sup>, J. D. Nam<sup>47</sup>, Md. Nasim<sup>38</sup>, K. Nayak<sup>12</sup>, D. Neff<sup>25</sup>, J. M. Nelson<sup>32</sup>, D. B. Nemes<sup>22</sup>, M. Nie<sup>28</sup>, G. Nigmatkulov<sup>11</sup>, T. Niida<sup>40</sup>, R. Nishitani<sup>40</sup>, L. V. Nogach<sup>3</sup> T. Nonaka<sup>40</sup>, A. S. Nunes<sup>3</sup>, G. Odyniec<sup>24</sup>, A. Ogawa<sup>3</sup>, S. Oh<sup>24</sup>, V. A. Okorokov<sup>11</sup>, K. Okubo<sup>40</sup>, B. S. Page<sup>3</sup>, R. Pak<sup>3</sup>, J. Pan<sup>2</sup>, A. Pandav<sup>53</sup>, A. K. Pandey<sup>40</sup>, Y. Panebratsev<sup>7</sup>, P. Parfenov<sup>11</sup>,

A. Paul<sup>15</sup>, B. Pawlik<sup>56</sup>, D. Pawlowska<sup>27</sup>, C. Perkins<sup>32</sup>, J. Pluta<sup>27</sup>, B. R. Pokhrel<sup>47</sup>, J. Porter<sup>24</sup>, M. Posik<sup>47</sup>, V. Prozorova<sup>19</sup>, N. K. Pruthi<sup>8</sup>, M. Przybycien<sup>4</sup>, J. Putschke<sup>37</sup>, H. Qiu<sup>50</sup>, A. Quintero<sup>47</sup>, C. Racz<sup>15</sup>, S. K. Radhakrishnan<sup>13</sup>, N. Raha<sup>37</sup>, R. L. Ray<sup>54</sup>, R. Reed<sup>42</sup>, H. G. Ritter<sup>24</sup> M. Robotkova<sup>20</sup>, J. L. Romero<sup>23</sup>, D. Roy<sup>25</sup>, L. Ruan<sup>3</sup>, A. K. Sahoo<sup>38</sup>, N. R. Sahoo<sup>28</sup>, H. Sako<sup>40</sup>, S. Salur<sup>55</sup>, E. Samigullin<sup>10</sup>, J. Sandweiss<sup>22,67</sup>, S. Sato<sup>40</sup>, W. B. Schmidke<sup>3</sup>, N. Schmitz<sup>57</sup>, B. R. Schweid<sup>17</sup>, F. Seck<sup>46</sup>, J. Seger<sup>58</sup>, R. Seto<sup>15</sup>, P. Seyboth<sup>57</sup>, N. Shah<sup>59</sup>, E. Shahaliev<sup>7</sup>, P. V. Shanmuganathan<sup>3</sup>, M. Shao<sup>30</sup>, T. Shao<sup>29</sup>, R. Sharma<sup>49</sup>, A. I. Sheikh<sup>13</sup>, D. Y. Shen<sup>2</sup> S. S. Shi<sup>12</sup>, Y. Shi<sup>28</sup>, Q. Y. Shou<sup>29</sup>, E. P. Sichtermann<sup>24</sup>, R. Sikora<sup>4</sup>, J. Singh<sup>8</sup>, S. Singha<sup>50</sup> P. Sinha<sup>49</sup>, M. J. Skoby<sup>44,60</sup>, N. Smirnov<sup>22</sup>, Y. Söhngen<sup>35</sup>, W. Solyst<sup>51</sup>, Y. Song<sup>22</sup>, H. M. Spinka<sup>61,68</sup>, B. Srivastava<sup>44</sup>, T. D. S. Stanislaus<sup>48</sup>, M. Stefaniak<sup>27</sup>, D. J. Stewart<sup>22</sup>, M. Strikhanov<sup>1</sup> B. Stringfellow<sup>44</sup>, A. A. P. Suaide<sup>62</sup>, M. Sumbera<sup>20</sup>, X. M. Sun<sup>12</sup>, X. Sun<sup>41</sup>, Y. Sun<sup>30</sup>, Y. Sun<sup>63</sup>, B. Surrow<sup>47</sup>, D. N. Svirida<sup>10</sup>, Z. W. Sweger<sup>23</sup>, P. Szymanski<sup>27</sup>, A. H. Tang<sup>3</sup>, Z. Tang<sup>30</sup>, A. Taranenko<sup>11</sup>, T. Tarnowsky<sup>64</sup>, J. H. Thomas<sup>24</sup>, A. R. Timmins<sup>16</sup>, D. Tlusty<sup>58</sup>, T. Todoroki<sup>40</sup>, M. Tokarev<sup>7</sup>, C. A. Tomkiel<sup>42</sup>, S. Trentalange<sup>25</sup>, R. E. Tribble<sup>2</sup>, P. Tribedy<sup>3</sup>, S. K. Tripathy<sup>3</sup> T. Truhlar<sup>19</sup>, B. A. Trzeciak<sup>19</sup>, O. D. Tsai<sup>25</sup>, Z. Tu<sup>3</sup>, T. Ullrich<sup>3</sup>, D. G. Underwood<sup>48,61</sup>, I. Upsal<sup>38</sup> G. Van Buren<sup>3</sup>, J. Vanek<sup>20</sup>, A. N. Vasiliev<sup>11,36</sup>, I. Vassiliev<sup>52</sup>, V. Verkest<sup>37</sup>, F. Videbæk<sup>3</sup>, S. Vokal<sup>7</sup>, S. A. Voloshin<sup>37</sup>, F. Wang<sup>44</sup>, G. Wang<sup>25</sup>, J. S. Wang<sup>63</sup>, P. Wang<sup>30</sup>, X. Wang<sup>28</sup>, Y. Wang<sup>12</sup>, Y. Wang<sup>31</sup>, Z. Wang<sup>28</sup>, J. C. Webb<sup>3</sup>, P. C. Weidenkaff<sup>35</sup>, G. D. Westfall<sup>64</sup>, H. Wieman<sup>2</sup> S. W. Wissink<sup>51</sup>, R. Witt<sup>65</sup>, J. Wu<sup>12</sup>, J. Wu<sup>50</sup>, Y. Wu<sup>15</sup>, B. Xi<sup>21</sup>, Z. G. Xiao<sup>31</sup>, G. Xie<sup>24</sup>, W. Xie<sup>44</sup>, H. Xu<sup>63</sup>, N. Xu<sup>24</sup>, Q. H. Xu<sup>28</sup>, Y. Xu<sup>28</sup>, Z. Xu<sup>3</sup>, Z. Xu<sup>25</sup>, G. Yang<sup>28</sup>, C. Yang<sup>28</sup>, Q. Yang<sup>28</sup>, S. Yang<sup>66</sup>, Y. Yang<sup>26</sup>, Z. Ye<sup>39</sup>, Z. Ye<sup>41</sup>, L. Yi<sup>28</sup>, K. Yip<sup>3</sup>, Y. Yu<sup>28</sup>, H. Zbroszczyk<sup>27</sup>, W. Zha<sup>30</sup>, C. Zhang<sup>17</sup>, D. Zhang<sup>12</sup>, J. Zhang<sup>28</sup>, S. Zhang<sup>41</sup>, S. Zhang<sup>29</sup>, Y. Zhang<sup>50</sup>, Y. Zhang<sup>30</sup>, Y. Zhang<sup>12</sup>, Z. J. Zhang<sup>26</sup> Z. Zhang³, Z. Zhang⁴¹, F. Zhao⁵⁰, J. Zhao²⁰, M. Zhao³, C. Zhou²⁰, Y. Zhou¹², X. Zhu³¹, M. Zurek⁶¹ & M. Zvzak52

<sup>1</sup>The American University in Cairo, New Cairo, Egypt. <sup>2</sup>Texas A&M University, College Station, TX, USA. <sup>3</sup>Brookhaven National Laboratory, Upton, NY, USA. <sup>4</sup>Faculty of Physics and Applied Computer Science (FPACS), AGH University of Science and Technology, Kraków, Poland. <sup>5</sup>Ohio State University, Columbus, OH, USA. <sup>6</sup>University of Kentucky, Lexington, KY, USA. <sup>7</sup>Joint Institute for Nuclear Research, Dubna, Russia. <sup>8</sup>Panjab University, Chandigarh, India. <sup>9</sup>Variable Energy Cyclotron Centre, Kolkata, India. <sup>10</sup>Alikhanov Institute for Theoretical and Experimental Physics, NRC "Kurchatov Institute", Moscow, Russia. 11 National Research Nuclear University MEPhI, Moscow, Russia. <sup>12</sup>Central China Normal University, Wuhan, China. <sup>13</sup>Kent State University, Kent, OH, USA. <sup>14</sup>Instituto de Alta Investigación, Universidad de

Tarapacá, Arica, Chile. 15 University of California, Riverside, Riverside, CA, USA. 16 University of Houston, Houston, TX, USA. <sup>17</sup>State University of New York, Stony Brook, NY, USA. <sup>18</sup>University of Jammu, Jammu, India. 19 Faculty of Nuclear Sciences and Physical Engineering (FNSPE), Czech Technical University in Prague, Prague, Czech Republic. 20 Nuclear Physics Institute of the CAS, Rež, Czech Republic. <sup>21</sup>Shanghai Institute of Applied Physics, Chinese Academy of Sciences, Shanghai, China. <sup>22</sup>Yale University, New Haven, CT, USA. <sup>23</sup>University of California, Davis, Davis, CA, USA. 24 Lawrence Berkeley National Laboratory, Berkeley, CA, USA. <sup>25</sup>University of California, Los Angeles, Los Angeles, CA, USA. <sup>26</sup>National Cheng Kung University, Tainan, Taiwan. 27 Warsaw University of Technology, Warsaw, Poland. 28 Shandong University, Qingdao, China. <sup>29</sup>Fudan University, Shanghai, China. <sup>30</sup>University of Science and Technology of China, Hefei, China. 31 Tsinghua University, Beijing, China. 32 University of California, Berkeley, Berkeley, CA, USA. 33 Eötvös Loránd University (ELTE), Budapest, Hungary. <sup>34</sup>Abilene Christian University, Abilene, TX, USA. <sup>35</sup>Heidelberg University, Heidelberg, Germany. <sup>36</sup>Institute of High Energy Physics, NRC "Kurchatov Institute", Protvino, Russia. <sup>37</sup>Wayne State University, Detroit, MI, USA. <sup>38</sup>Indian Institute of Science Education and Research (IISER), Berhampur, India. 39Rice University, Houston, TX, USA. 40University of Tsukuba, Tsukuba, Japan. <sup>41</sup>University of Illinois Chicago, Chicago, IL, USA. <sup>42</sup>Lehigh University, Bethlehem, PA, USA. 43 University of Calabria & INFN-Cosenza, Cosenza, Italy. 44 Purdue University, West Lafayette, IN, USA. 45 Southern Connecticut State University, New Haven, CT, USA. <sup>48</sup>Technische Universität Darmstadt, Darmstadt, Germany. <sup>47</sup>Temple University, Philadelphia, PA, USA. <sup>48</sup>Valparaiso University, Valparaiso, IN, USA. <sup>49</sup>Indian Institute of Science Education and Research, Tirupati (IISER Tirupati), Tirupati, India. 50 Institute of Modern Physics, Chinese Academy of Sciences, Lanzhou, China. 51 Indiana University Bloomington, Bloomington, IN, USA. 52 Frankfurt Institute for Advanced Studies (FIAS), Frankfurt, Germany. 53 National Institute of Science Education and Research (NISER), Homi Bhabha National Institute (HBNI), Jatani, India. 54 University of Texas at Austin, Austin, TX, USA. 55 Rutgers University, Piscataway, NJ, USA. 56 Institute of Nuclear Physics PAN, Kraków, Poland. 57 Max Planck Institut für Physik, Munich, Germany. 58 Creighton University, Omaha, NE, USA. <sup>59</sup>Indian Institute of Technology Patna, Patna, India. <sup>60</sup>Ball State University, Muncie, IN, USA. <sup>61</sup>Argonne National Laboratory, Lemont, IL, USA. <sup>62</sup>Universidade de São Paulo, São Paulo, Brazil. <sup>63</sup>Huzhou University, Huzhou, China. <sup>64</sup>Michigan State University, East Lansing, MI, USA. <sup>65</sup>United States Naval Academy, Annapolis, MD, USA. <sup>66</sup>South China Normal University, Guangzhou, China. 67Deceased: J. Sandweiss. 68Deceased: H. M. Spinka. <sup>™</sup>e-mail: star-publication@bnl.gov

#### **Methods**

#### **Data description**

This φ-meson  $\rho_{00}$  analysis is based on Au+Au collisions at  $\sqrt{s_{NN}}$  = 11.5, 19.6, 27, 39, 62.4 and 200 GeV, with samples of 8, 19, 348, 117, 45 and 1,560 million events, respectively. For K\*0 mesons, the sample sizes are 12, 18, 36, 70, 130, 520 and 350 million events at  $\sqrt{s_{NN}}$  = 11.5, 14.5, 19.6, 27, 39, 54.4 and 200 GeV, respectively. All data were taken using a minimum-bias trigger. This trigger selects all particle-producing collisions regardless of the extent of overlap of the incident nuclei. To maximize the statistics and ensure uniform acceptance, a selection on the position of the reconstructed primary vertex along the beam axis  $(V_z)$  is made for each of the energies. In the case of the  $\phi$  analysis,  $V_z$  is required to be within  $\pm 30$  cm of the centre of the STAR TPC<sup>31</sup> for  $\sqrt{s_{\rm NN}}$  = 200 GeV , whereas the corresponding  $V_z$  windows are  $\pm 40, 40, 70, 70$  and 50 cm at beam energies of 62.4, 39, 27, 19.6 and 11.5 GeV, respectively. For  $K^{*0}$ , the  $V_z$  window is ±50 cm at 39 GeV and below and ±30 cm at the remaining beam energies. Charged particles with pseudorapidities  $|\eta|$  < 1.0 are reconstructed using the TPC. For both analyses, the centrality definition is based on the raw charged-particle multiplicity in the TPC within  $|\eta|$  < 0.5. The primary vertex position in the plane that is transverse to the direction of the colliding Au ion beams,  $V_n$  is required to be within 2 cm of the peak of the reconstructed primary vertex position for all energies except 14.5 GeV. For 14.5 GeV, the vertex is not centred at (0,0) in the xy plane and slightly offset at (0.0, -0.89) cm, and the  $|V_r| = \sqrt{V_x^2 + (V_y + 0.89)^2}$  is selected to be smaller than 1 cm to reject interactions with the beam pipe.

#### Reconstruction of the event plane

In this paper, we follow the same procedure as in a previous study of the STAR Collaboration  $^{30}$ , by using the second-order event plane based on tracks in the TPC as a proxy for the event reaction plane.  $\varphi$  and  $K^{*0}$  daughter candidates were excluded from the event-plane determination, to avoid self-correlation between the event plane and those particles under study. Furthermore, results obtained using the first-order event plane are presented in this section for the  $\varphi$  global spin alignment. The first-order event plane is based on the shower maximum detectors of the zero-degree calorimeters  $^{44}$  for the  $\sqrt{s_{\rm NN}}=62.4$  and 200-GeV data and on the beam-beam counter  $^{45,46}$  for the lower energies.

In non-central collisions, a fraction of the initial angular momentum is carried away by spectator nucleons and, therefore, the normal to the first-order event plane can be more sensitive to the direction of the initial global angular momentum than that for the second-order event plane. On the other hand, the resolution of the second-order event plane, based on the TPC tracking, is better than that of the first-order event plane, owing to the large multiplicity and elliptic flow<sup>24</sup> within the TPC acceptance near middle rapidity. As discussed in ref. <sup>47</sup>, when all corrections are taken into account, the two measurements should agree with each other to the first approximation, as demonstrated below. Uncertainties in the event-plane resolution are negligible relative to the statistical and systematic uncertainties of the final results.

#### φ-meson and K\*0-meson yield extraction

The distributions of  $\varphi$  and  $K^{*0}$  invariant mass are obtained for each  $p_T$ , centrality and  $\cos\theta^*$  bin. The corresponding combinatorial background for the  $\varphi$  meson is estimated by event mixing, that is, creating  $(K^*, K^-)$  pairs from tracks selected from different events with the same centrality, event-plane angle bin and primary vertex bin. For  $K^{*0}$  mesons, the background is estimated by rotating the momentum vector of one of the decay daughters by  $180^\circ$ . Both techniques can effectively break the correlation between pairs in real events and the results from the two techniques are consistent within about  $1.0-1.5\sigma$ . Invariant-mass yields are then obtained by subtracting the corresponding backgrounds. Small, residual backgrounds remain, owing to particle misidentification for both techniques and to non-resonance correlations for the rotation technique. The upper panels of Extended Data Fig. 1 show typical combinatorial-background-subtracted  $\varphi$  and  $K^{*0}$ 

invariant-mass distributions integrated over  $\cos\theta^*$ . The extracted yield is fitted with a Breit–Wigner function for the signal plus a second-order polynomial curve for the residual background. The lower panels of Extended Data Fig. 1 show examples of  $\varphi$  and  $K^{*0}$  yield as a function of  $\cos\theta^*$ . This yield, after correction for detection efficiency and acceptance at each  $p_{\rm T}$  and centrality, is then used to extract  $\rho_{00}$ .

# Corrections for finite event-plane resolution, efficiency and acceptance

φ-meson  $ρ_{00}$  analysis. Detector efficiency within the acceptance is corrected using the STAR Monte Carlo embedding method <sup>48-50</sup>. To account for finite event-plane resolution and finite acceptance in pseudorapidity  $(η)^{51}$ , the observed  $cos θ^*$  distribution is not fitted using equation (1) but is instead described by the correction procedure derived in ref. <sup>47</sup>, wherein the data are fitted using

$$\left[\frac{dN}{d\cos\theta^*}\right]_{|\eta|} \propto \left(1 + \frac{B'F}{2}\right) + (A' + F)\cos^2\theta^* + \left(A'F - \frac{B'F}{2}\right)\cos^4\theta^*,$$
(2)

in which

$$A' = \frac{A(1+3R)}{4+A(1-R)}, \quad B' = \frac{A(1-R)}{4+A(1-R)}, \tag{3}$$

and

$$A = \frac{3\rho_{00} - 1}{1 - \rho_{00}},\tag{4}$$

and F is a factor that accounts for finite acceptance. Its value depends on  $p_{\rm T}$  and  $\eta$  and is calculated using a simulation<sup>47</sup>. The factor R accounts for finite event-plane resolution. For the first-order event plane, it is  $R_1 = \langle \cos 2(\Psi_r - \Psi_1) \rangle$ , in which  $\Psi_1$  is the first-order event plane and  $\Psi_r$  is the true reaction plane.  $R_1$  can be obtained following the usual procedure in flow analyses<sup>24</sup>. For the second-order event plane, R is replaced by  $R_{21} = \langle \cos 2(\Psi_1 - \Psi_2) \rangle / R_1$ , in which  $\Psi_2$  is the second-order event plane. Extended Data Figure 2 shows an example of such fitting. The fitting procedure has been repeated with different n acceptance cuts for the decay daughters, namely |n| < 1 and |n| < 0.6, and results after correction converge as expected, as seen in simulations<sup>47</sup>. In this procedure, the corrections for detector efficiency and acceptance are applied separately. Performing the procedure this way provides insight into the effect of acceptance alone, and the effect of acceptance can be taken into account with a high precision. In practice, this procedure has been verified to give results consistent with those from the procedure below. It is worth noting that, in simulation studies, we found that the decay-topology-dependentefficiency along with the elliptic flow  $(v_2)^{24}$  of the parent meson can bias the  $\rho_{00}$  measurements. Such effects have been fully corrected with the procedure of efficiency correction, for both  $\phi$  and  $K^{*0}$ .

 $K^{*0}$ -meson  $\rho_{oo}$  analysis. The detector acceptance and efficiency are calculated using the STAR Monte Carlo embedding method  $^{48-50}$ . In this process, a small extra fraction of  $K^{*0}$  mesons (5%) is generated with a uniform distribution in the rapidity range [–1, 1], transverse momentum range [0, 10 GeV c $^{-1}$ ] and azimuthal angle range [0, 2 $\pi$ ], and then passed through the STAR detector simulation in GEANT3 (ref.  $^{52}$ ). The number of  $K^{*0}$  mesons reconstructed after passing through the detector simulation and through the same set of track selections as used in real data, compared with the input number of  $K^{*0}$  mesons within the same rapidity interval, gives the reconstruction efficiency × acceptance ( $\epsilon_{\rm rec}$ ). The yield, after correction for reconstruction efficiency × acceptance, is fitted with

$$\frac{dN}{d(\cos\theta^*)} \propto (1 - \rho_{00}^{\text{obs}}) + (3\rho_{00}^{\text{obs}} - 1)\cos^2\theta^*$$
 (5)

to extract  $\rho_{00}^{\text{obs}}$ , in which 'obs' stands for 'observed'. Extended Data Figure 3 shows an example of such fitting. The  $\rho_{00}^{\text{obs}}$  is then corrected for finite event-plane resolution (R), following the procedure laid out in ref. <sup>47</sup>, to obtain the final  $\rho_{00}$ ,

$$\rho_{00} - \frac{1}{3} = \frac{4}{1 + 3R} \left( \rho_{00}^{\text{obs}} - \frac{1}{3} \right). \tag{6}$$

The stability of the embedding correction is validated by repeating the analysis with the previous procedure, and both procedures give consistent results.

#### Consistency check using the first-order event plane

In Extended Data Fig. 4, the  $\rho_{00}$  of  $\varphi$  mesons at  $p_T > 1.2$  GeV  $c^{-1}$  is presented for Au+Au collisions at  $\sqrt{s_{\rm NN}} = 11.5$ , 19.6, 27, 39, 62.4 and 200 GeV. For  $1.2 < p_T < 5.4$  GeV  $c^{-1}$ ,  $\rho_{00}$  averaged over energies of 62.4 GeV and below is  $0.3565 \pm 0.0037$  (stat.)  $\pm 0.0042$  (syst.) for the first-order event plane and  $0.3512 \pm 0.0017$  (stat.)  $\pm 0.0017$  (syst.) for the second-order event plane. The former has a larger error than the latter, owing to its lower event-plane resolution. Taking the total uncertainty as the quadrature sum of statistical and systematic errors, the two measurements are consistent with each other within about  $2\sigma$ . Both measurements indicate strong global spin alignment with a  $4.2\sigma$  (first-order event plane) and  $7.4\sigma$  (second-order event plane) significance. For K\*0, the first-order event-plane result is not presented because the statistical errors are too large owing to the lower first-order event-plane resolution.

#### Self-consistency check with randomly oriented $\hat{L}$

As a self-consistency check for the procedure, we also repeated both analyses with the  $\hat{L}$  direction randomly oriented in space, for which any global spin alignment would be eliminated and  $\rho_{00}$  should be 1/3. Our exercise with randomly oriented  $\hat{L}$  gives 0.3378  $\pm$  0.0016 (stat.)  $\pm$  0.0010 (syst.) for the  $\varphi$  meson and 0.3369  $\pm$  0.0086 (stat.)  $\pm$  0.0053 (syst.) for  $K^{*0}$  (averaged over beam energies of 62.4 GeV and below).

#### Global spin alignment in the in-plane direction

Extended Data Figure 5 shows  $\rho_{00}$  for  $\Phi$  with two choices of quantization axes that are perpendicular to each other, namely  $\hat{L}$  and  $\hat{b}$ , corresponding to the out-of-plane and the in-plane directions, respectively.  $\hat{L}$  is the usual choice of quantization axis and is used everywhere else in this paper. Note that, although the direction of  $\hat{b}$  is rotated 90° about the beam axis relative to  $\hat{L}$  in the ideal case, the  $\theta^*$  angles obtained with  $\hat{b}$  and  $\hat{L}$  do not differ by 90° in general. Thus their  $\rho_{00}$  cannot be mapped to each other by a trivial relationship. The plot shows that  $\rho_{00}$  in the out-of-plane direction is considerably larger than in the in-plane direction, which can be attributed to the effect of elliptic flow<sup>5</sup>.

#### Transverse momentum dependence

Extended Data Figures 6 and 7 show  $\rho_{00}$  as a function of transverse momentum (150 <  $p_{\rm T}$  < 400 MeV c<sup>-1</sup>), the TPC tracking efficiency increases steeply with increasing  $p_{\rm T}$  and, consequently, there is a bias against a daughter kaon pairing with another kaon from the adjacent phase space. This constraint in forming pairs introduces a notable artificial  $\phi$ -meson  $\rho_{00}$  at relatively low  $p_{\rm T}$  that is difficult to correct. For that reason,  $\rho_{00}$  for  $\phi$  mesons is presented for  $p_{\rm T}$  > 1.2 GeV c<sup>-1</sup> only, in which the aforementioned effect diminishes and measurements are reliable, as confirmed by simulation studies. For a similar reason,  $\rho_{00}$  for K\*0 is shown for  $p_{\rm T}$  > 1.0 GeV c<sup>-1</sup> only. For all energies considered, we see that the departure of  $\rho_{00}$  from 1/3 for the  $\phi$  meson occurs mainly at  $p_{\rm T}$  within about 1.0–2.4 GeV c<sup>-1</sup> and, at larger  $p_{\rm T}$ , the result can be considered consistent with 1/3 within about 2 $\sigma$  or less. The measurement of

energy and centrality dependence shown in this paper were obtained by averaging  $\rho_{00}(p_T)$  discussed in this subsection for the corresponding centrality and  $p_T$  range with  $1/(\text{stat. error})^2$  as weight. We compared the  $\rho_{00}$  value for the  $\phi$  meson at 27 GeV (our best statistical data point) to the yield-weighted average and the difference is negligible.

#### Centrality dependence

Extended Data Figure 8 shows  $\rho_{00}$  as a function of centrality at selected energies, for  $\phi$  (upper panels) and  $K^{*0}$  (lower panels). The  $p_T$  range for taking the average value for  $\phi$  is 1.2 <  $p_T$  < 5.4 GeV c<sup>-1</sup> and that for K\*0 is  $1.0 < p_T < 5.0 \text{ GeV } c^{-1}$ . At high energies (62.4 GeV and above for  $\phi$  mesons and 39 GeV and above for  $K^{*0}$ ),  $\rho_{00}$  in central collisions tends to be less than 1/3. This might be caused by transverse local spin alignment<sup>26</sup> and/ or a contribution from the helicity polarization of quarks<sup>27</sup>, which tend to reduce  $\rho_{00}$ . This reduction in central collisions is further examined by plotting  $\rho_{00}$  as a function of energy for central collisions, as shown in Extended Data Fig. 9. We see that the  $\rho_{00}$  of  $\varphi$  mesons for 0–20% central collisions decreases with increasing energy and deviates below 1/3 with marginal significance at  $\sqrt{s_{NN}} = 200$  GeV. The  $p_T$  and centrality dependence of the large  $\rho_{00}$  signal is recently described by an improved version of the model with φ-meson field<sup>5</sup>. In this revised work, instead of considering a static meson, the global spin alignment is first derived from the spin Boltzmann equation in the rest frame of the  $\phi$  meson and then transformed into the laboratory frame with known momentum.

#### Global and local spin alignment

In heavy-ion collisions, the global spin alignment for a collision system can show up in local spin alignments as well. It is the same phenomenon but viewed from different frames. For example, the relation between global  $\rho_{00}$  and production plane  $\rho_{00}\{PP\}$  is given<sup>33</sup> by  $\rho_{00}\{PP\}-\frac{1}{3}=\left(\rho_{00}-\frac{1}{3}\right)^{\frac{1+3\nu_2}{4}}$ . Here the production plane is the plane defined by the plane of  $\rho_{00}\{PP\}$ . ned by the beam and the momentum direction of the vector meson and the  $\rho_{00}$ {PP} is measured with the normal to the production plane as the quantization axis. Another popular choice of local frame is the helicity frame, in which the momentum direction of the vector meson is taken as the quantization axis. An analytical relation between the global  $\rho_{00}$  and the helicity frame  $\rho_{00}$  does not exist but, based on our simulation for the same kinematic range, typical values of  $\rho_{00}$  in the helicity frame (between 0.2 and 0.6 (ref. 53)) will result in the global  $\rho_{00}$ deviating from 1/3 by only about 0.001 and about 0.01 for  $\Phi$  and  $K^{*0}$ mesons, respectively, which are either negligible or very small when compared with the ( $\rho_{00}$  – 1/3) observations presented in this work. In a recent work, it is argued that the gradient of the radial flow along the beam axis can generate transverse vorticity loops at finite rapidity and cause the transverse local spin alignment<sup>26</sup>. This effect can give a negative contribution to the global spin alignment of vector mesons and is more prominent and clearly evident in central collisions. This can be part of the reason why, at top RHIC energies, we observe that the central value of  $\rho_{00}$  is below 1/3.

#### The result with $\hat{L}$ boosted into the rest frame of the vector meson

In the study of the hyperon global polarization or the vector meson global spin alignment, it is a convention to take  $\hat{L}$  in the laboratory frame as the quantization axis. We follow that convention in this paper. An alternative choice of the quantization axis is the direction of  $\hat{L}$  after being boosted into the rest frame of the particle<sup>54</sup>. We estimated that, for our  $\rho_{00}$  value that is averaged over beam energies of 62.4 GeV and below, the difference between the results with and without boosting  $\hat{L}$  into the rest frame is on the order of  $10^{-3}$ .

#### Taking the average value of 62.4 GeV and below

For both  $\phi$  and K\*0, the averaged  $\rho_{00}$  value of 62.4 GeV and below is obtained by taking the average with  $1/(\text{stat. error})^2$  as the weight for each energy.

#### Systematic error

For each beam energy, sources of systematic uncertainty can be categorized as: (1) quality selections at the event and track level, (2) particle identification cuts. (3) several invariant mass fitting ranges and residual background functions (first-order and second-order polynomials) for signal extraction, (4) histogram bin counting versus functional integration for yield extraction and (5) different efficiency evaluation methods. After repeating the analysis with reasonable variations of quality selections or analysis procedures and obtaining the corresponding values, systematic errors from each individual source are calculated as (maximum value – minimum value)/ $\sqrt{12}$ , assuming uniform probability distributions between the maximum and minimum values. The final systematic errors are the quadrature sum of the systematic errors from the various sources. The averaged  $\rho_{00}$  over beam energies of 62.4 GeV and below is calculated for each variation. The systematic errors for averaged  $\rho_{00}$  are evaluated with the same procedure as described above. Contributions of each systematic uncertainty for the averaged  $\rho_{00}$  are listed in Extended Data Tables 1 and 2 for  $\phi$  and  $K^{*0}$ , respectively.

#### **Data availability**

All raw data for this study were collected using the STAR detector at Brookhaven National Laboratory and are not available to the public. Derived data supporting the findings of this study are publicly available in the HEPData repository (https://www.hepdata.net/record/129067) or from the corresponding author on request.

#### **Code availability**

Codes to process raw data collected by the STAR detector and codes to analyse the produced data are not available to the public.

 Adler, C. et al. The RHIC zero degree calorimeters. Nucl. Instrum. Methods Phys. Res. A 470, 488–499 (2001).

- Whitten, C. A. The beam-beam counter: a local polarimeter at STAR. AIP Conf. Proc. 980, 390–396 (2008).
- Allgower, C. E. et al. The STAR endcap electromagnetic calorimeter. Nucl. Instrum. Methods Phys. Res. A 499, 740–750 (2003).
- Tang, A. H., Tu, B. & Zhou, C. S. Practical considerations for measuring global spin alignment of vector mesons in relativistic heavy ion collisions. *Phys. Rev. C* 98, 044907 (2018).
- Abelev, B. et al. Identified particle production, azimuthal anisotropy, and interferometry measurements in Au + Au collisions at √s<sub>NN</sub> = 9.2 GeV. Phys. Rev. C 81, 024911 (2010).
- 49. Adams, J. et al.  $K(892)^*$  resonance production in Au+Au and p+p collisions at  $\sqrt{s_{NN}}$  = 200 GeV. Phys. Rev. C 71, 064902 (2005).
- Aggarwal, M. M. et al. K\*0 production in Cu + Cu and Au + Au collisions at \( \sqrt{s\_{NN}} = 62.4 \) GeV and 200 GeV. Phys. Rev. C 84, 034909 (2011).
- Lan, S., Lin, Z.-W., Shi, S. & Sun, X. Effects of finite coverage on global polarization observables in heavy ion collisions. *Phys. Lett. B* 780, 319–324 (2018).
- 52. Fine, V. & Nevski, P. in Proc. 11th International Conference on Computing in High-Energy and Nuclear Physics 143–146 (2000).
- Chen, K.-B., Liang, Z.-T., Song, Y.-K. & Wei, S.-Y. Spin alignment of vector mesons in high energy pp collisions. Phys. Rev. D 102, 034001 (2020).
- Florkowski, W. & Ryblewski, R. Interpretation of Λ spin polarization measurements. Phys. Rev. C106. 024905 (2022).

Acknowledgements We thank the RHIC Operations Group and RCF at BNL, the NERSC Center at LBNL and the Open Science Grid Consortium for providing resources and support. This work was supported in part by the Office of Nuclear Physics within the U.S. DOE Office of Science, the U.S. National Science Foundation, National Natural Science Foundation of China, Chinese Academy of Sciences, the Ministry of Science and Technology of China and the Chinese Ministry of Education, the Higher Education Sprout Project by Ministry of Education at NCKU, the National Research Foundation of Korea, the Czech Science Foundation and Ministry of Education, Youth and Sports of the Czech Republic, the Hungarian National Research, Development and Innovation Office, New National Excellency Programme of the Hungarian Ministry of Human Capacities, Department of Atomic Energy and Department of Science and Technology of the Government of India, the National Science Centre of Poland, the Ministry of Science, Education and Sports of the Republic of Croatia, German Bundesministerium für Bildung, Wissenschaft, Forschung und Technologie (BMBF), Helmholtz Association, Ministry of Education, Culture, Sports, Science and Technology (MEXT) and Japan Society for the Promotion of Science (JSPS).

Author contributions All authors contributed extensively.

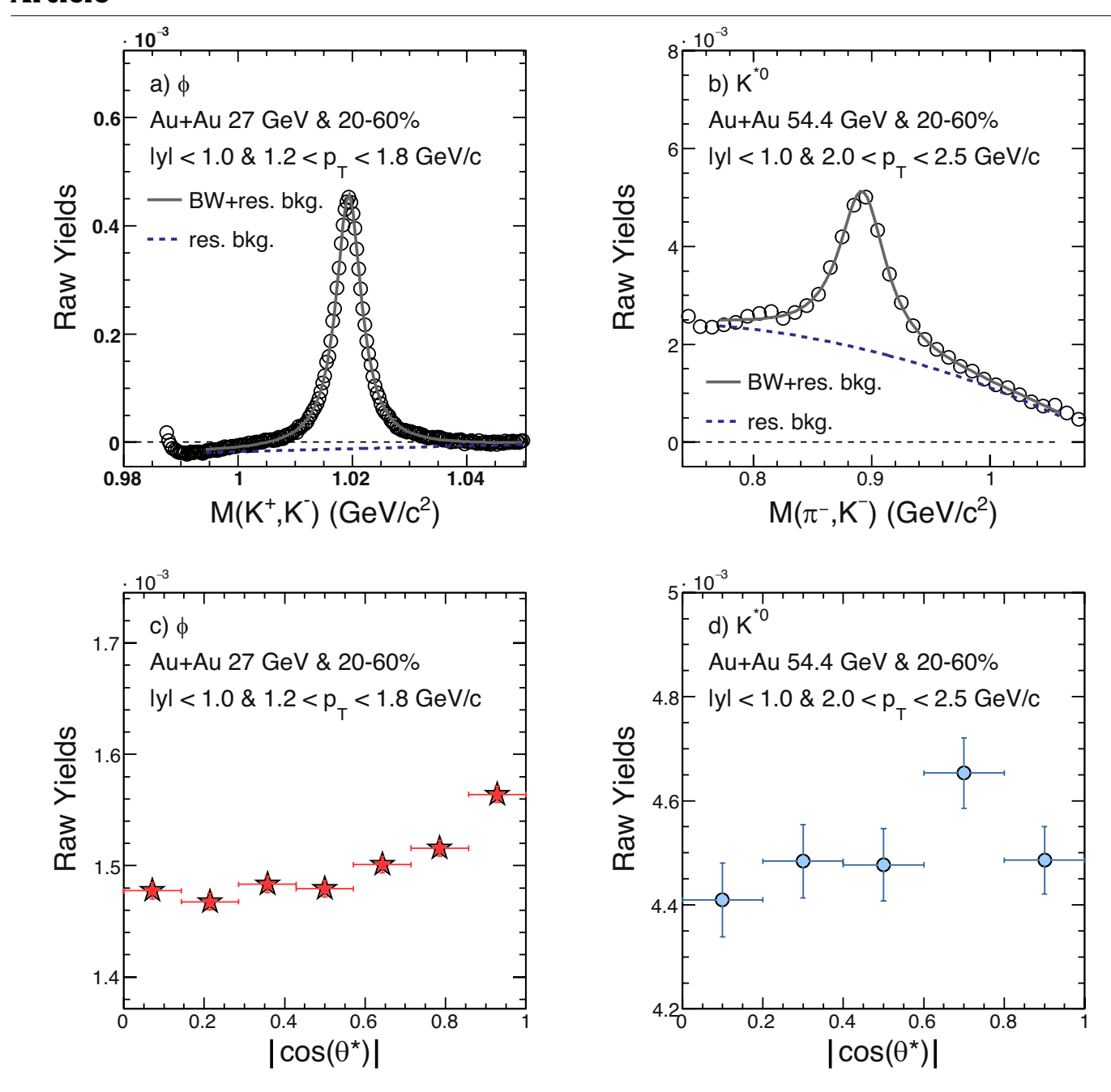
Competing interests The authors declare no competing interests.

#### Additional information

Correspondence and requests for materials should be addressed to the STAR Collaboration (star-publication@bnl.gov).

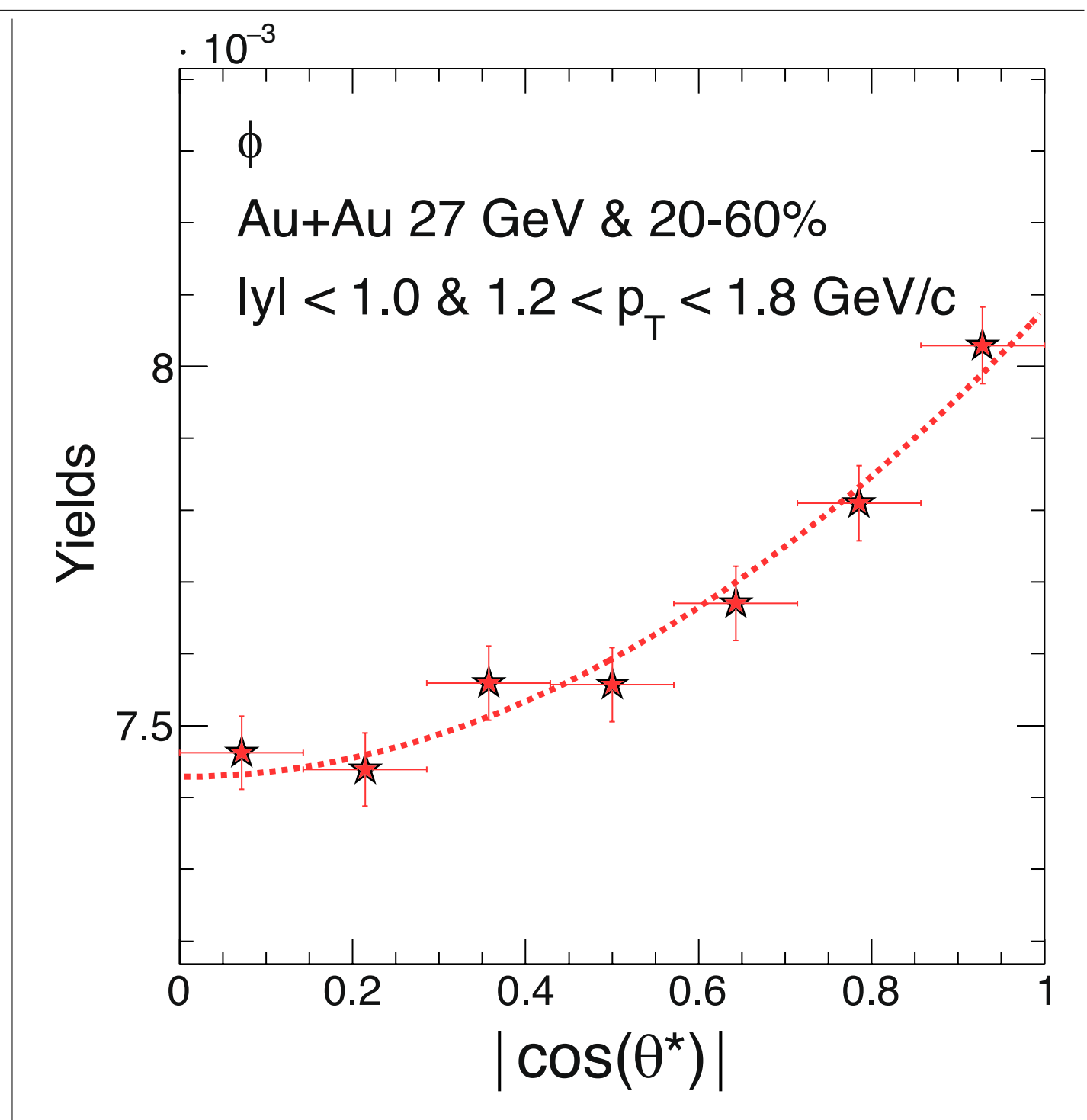
Peer review information Nature thanks Andrea Dainese, Ilya Selyuzhenkov and Xin-Nian Wang for their contribution to the peer review of this work.

Reprints and permissions information is available at http://www.nature.com/reprints.

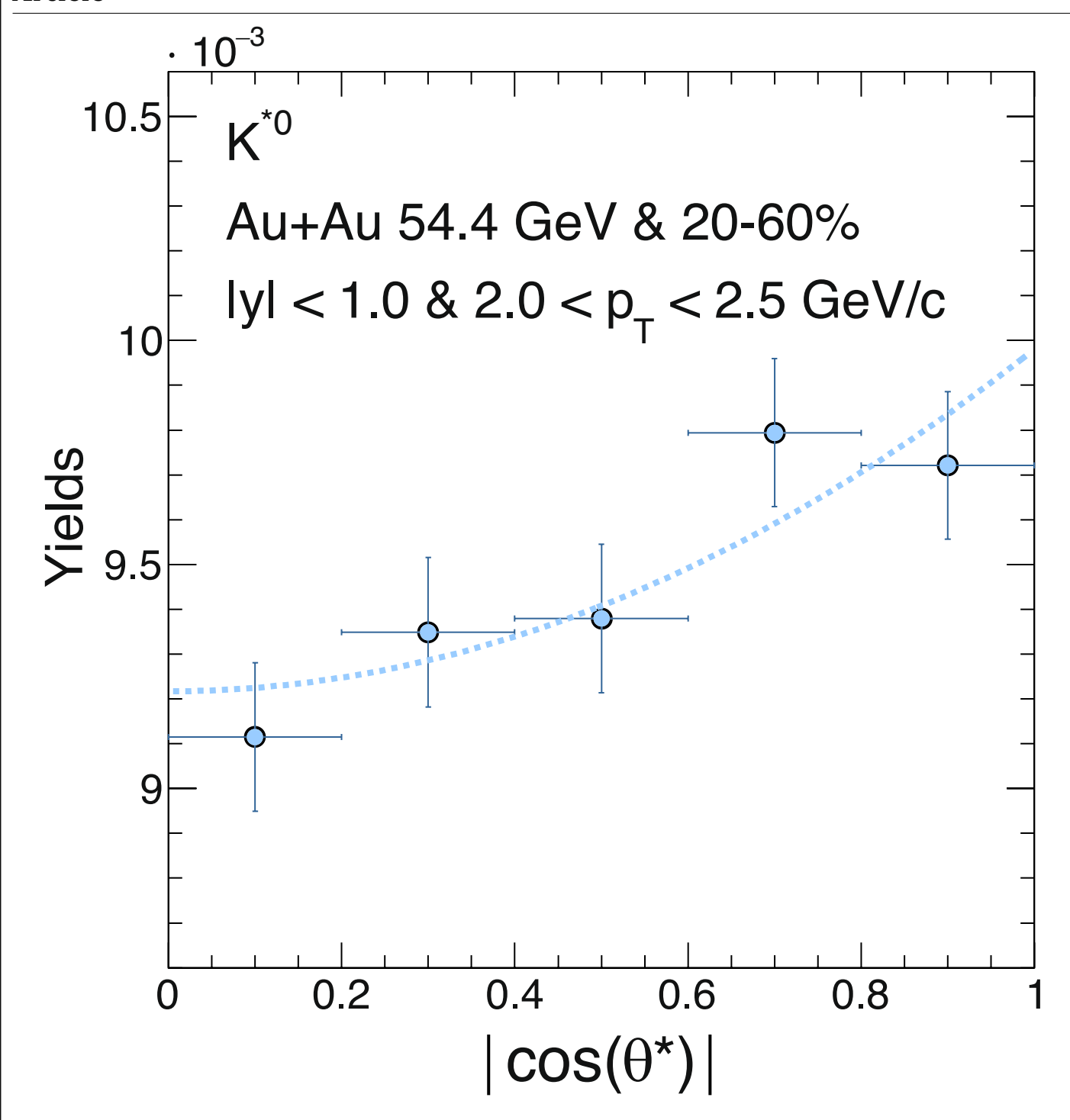


Extended Data Fig. 1 | Example of combinatorial-background-subtracted invariant-mass distributions and the extracted yields as a function of  $\cos\theta^*$  for  $\varphi$  and  $K^{*0}$  mesons. a, Example of  $\varphi \to K^* + K^-$  invariant-mass distributions, with combinatorial background subtracted, integrated over  $\cos\theta^*$ . b, Example

of  $K^{*0}$   $\to K^-\pi^+$  ( $K^+\pi^-$ ) invariant-mass distributions, with combinatorial background subtracted, integrated over  $\cos\theta^*$ . **c**, Extracted yields of  $\varphi$  as a function of  $\cos\theta^*$ . **d**, Extracted yields of  $K^{*0}$  as a function of  $\cos\theta^*$ .

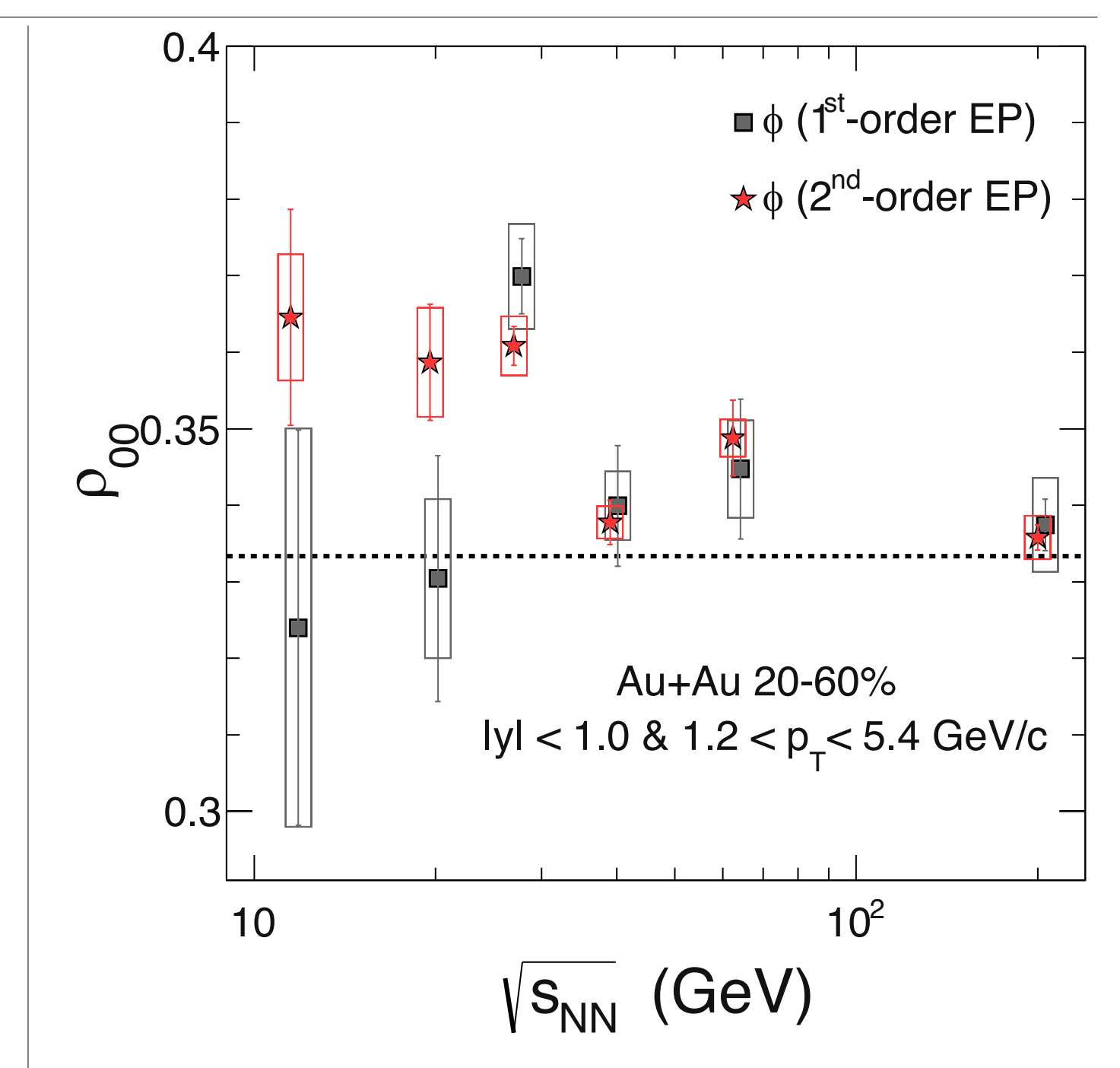


Extended Data Fig. 2 | Efficiency-corrected  $\phi$ -meson yields as a function of  $\cos\theta^*$  and corresponding fits with equation (2) in Methods. The red stars are efficiency-corrected yields for  $\phi$  mesons with |y| < 1.0 and  $1.2 < p_T < 1.8$  GeV  $c^{-1}$ , for 20-60% centrality at  $\sqrt{s_{NN}} = 27$  GeV.



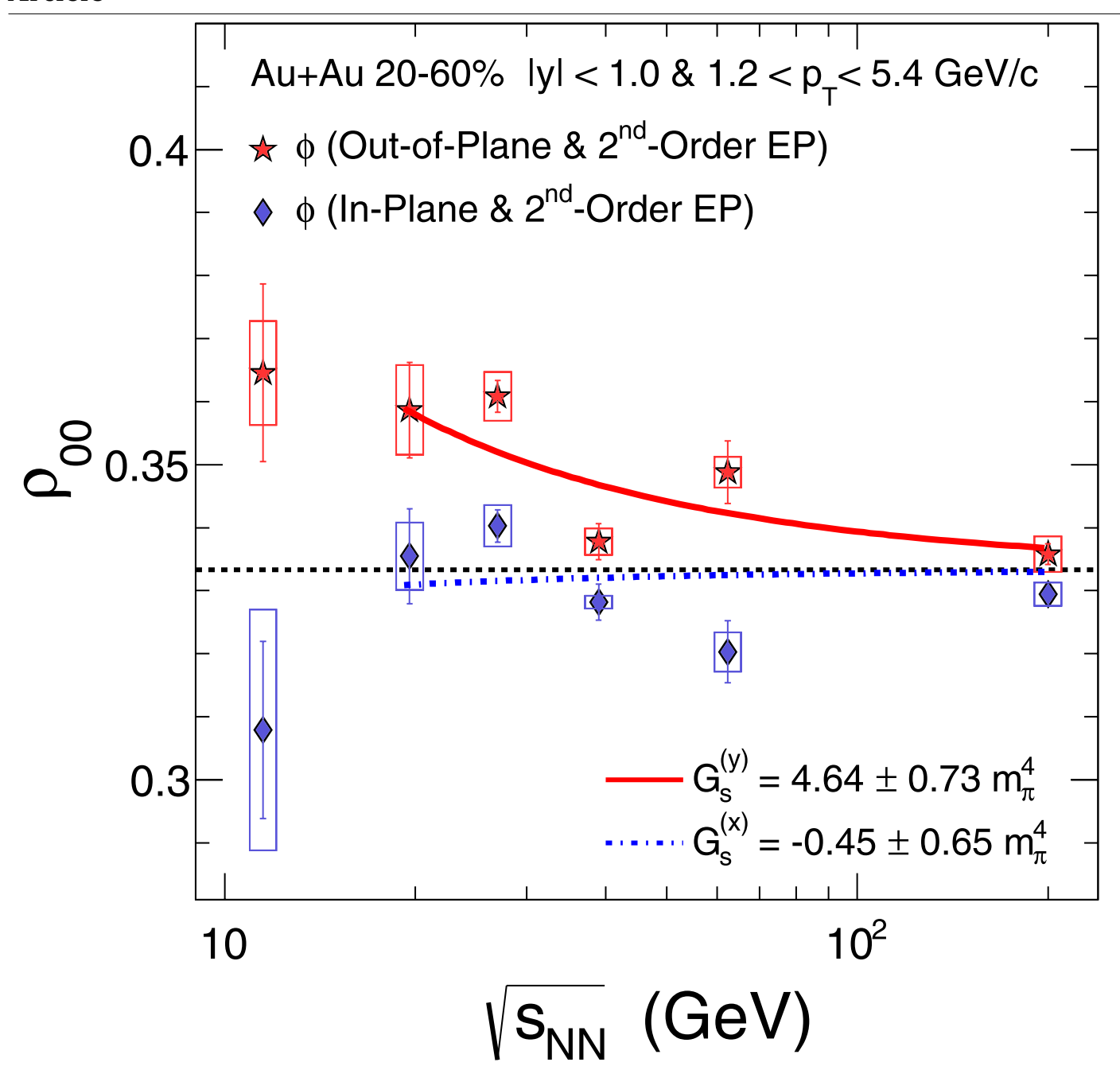
Extended Data Fig. 3 | Efficiency-corrected and acceptance-corrected  $K^{*0}$ -meson yields as a function of  $\cos\theta^*$  and corresponding fits with equation (5) in Methods. The blue circles are efficiency-corrected and

acceptance-corrected yields for K\*0 mesons with |y| < 1.0 and  $2.0 < p_T < 2.5$  GeV c<sup>-1</sup>, for 20-60% centrality at  $\sqrt{s_{NN}} = 54.4$  GeV.



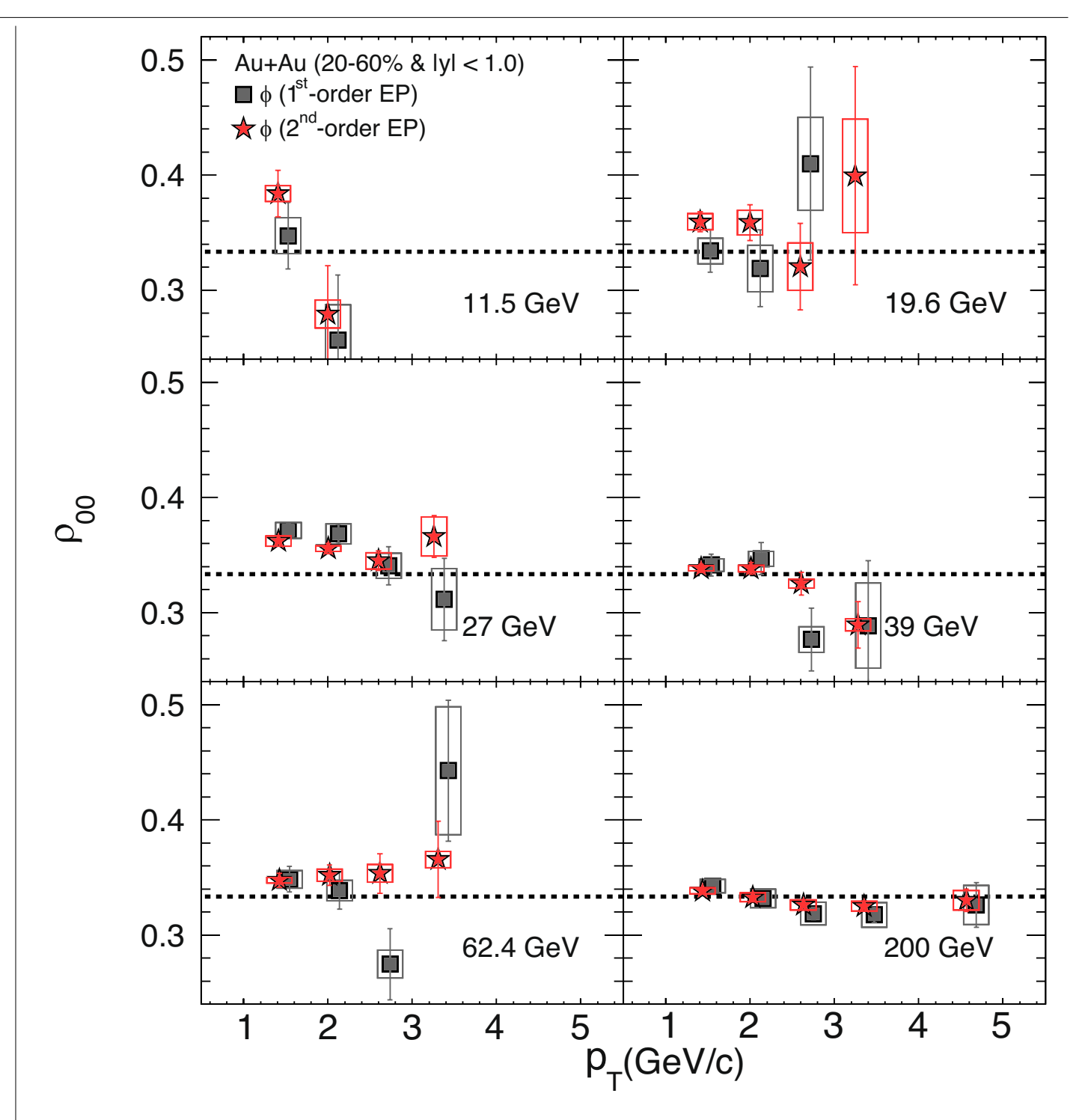
**Extended Data Fig. 4** |  $\phi$ -meson $\rho_{00}$  obtained from first-order and second-order event planes. The red stars (grey squares) show the  $\phi$ -meson  $\rho_{00}$  as a function of beam energy, obtained with the second-order (first-order) event plane.



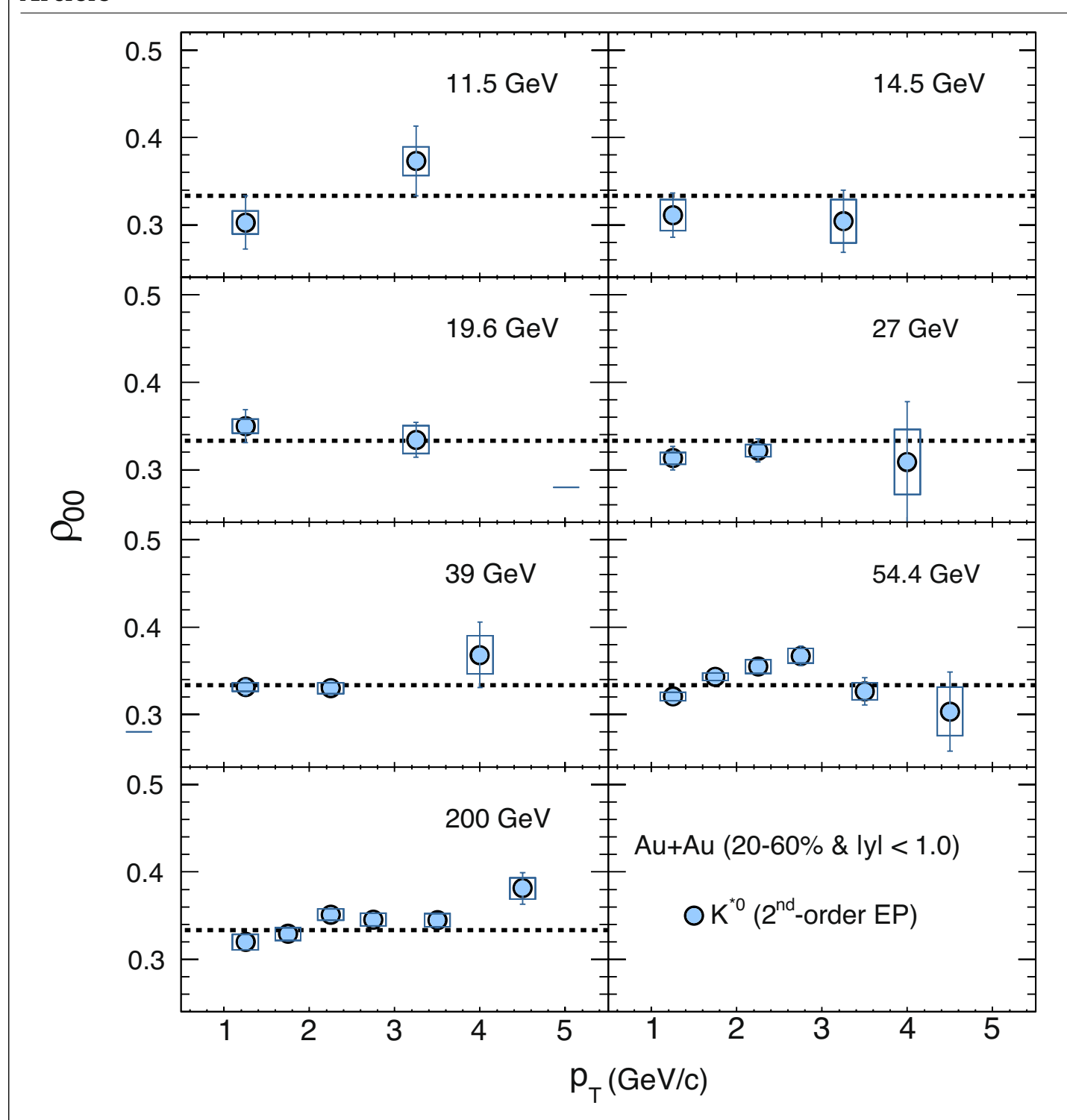


**Extended Data Fig. 5**  $| \Phi$ -meson  $\rho_{00}$  with respect to different quantization axes.  $\Phi$ -meson  $\rho_{00}$  as a function of beam energy, for the out-of-plane direction (stars) and the in-plane direction (diamonds). Curves are fits based on

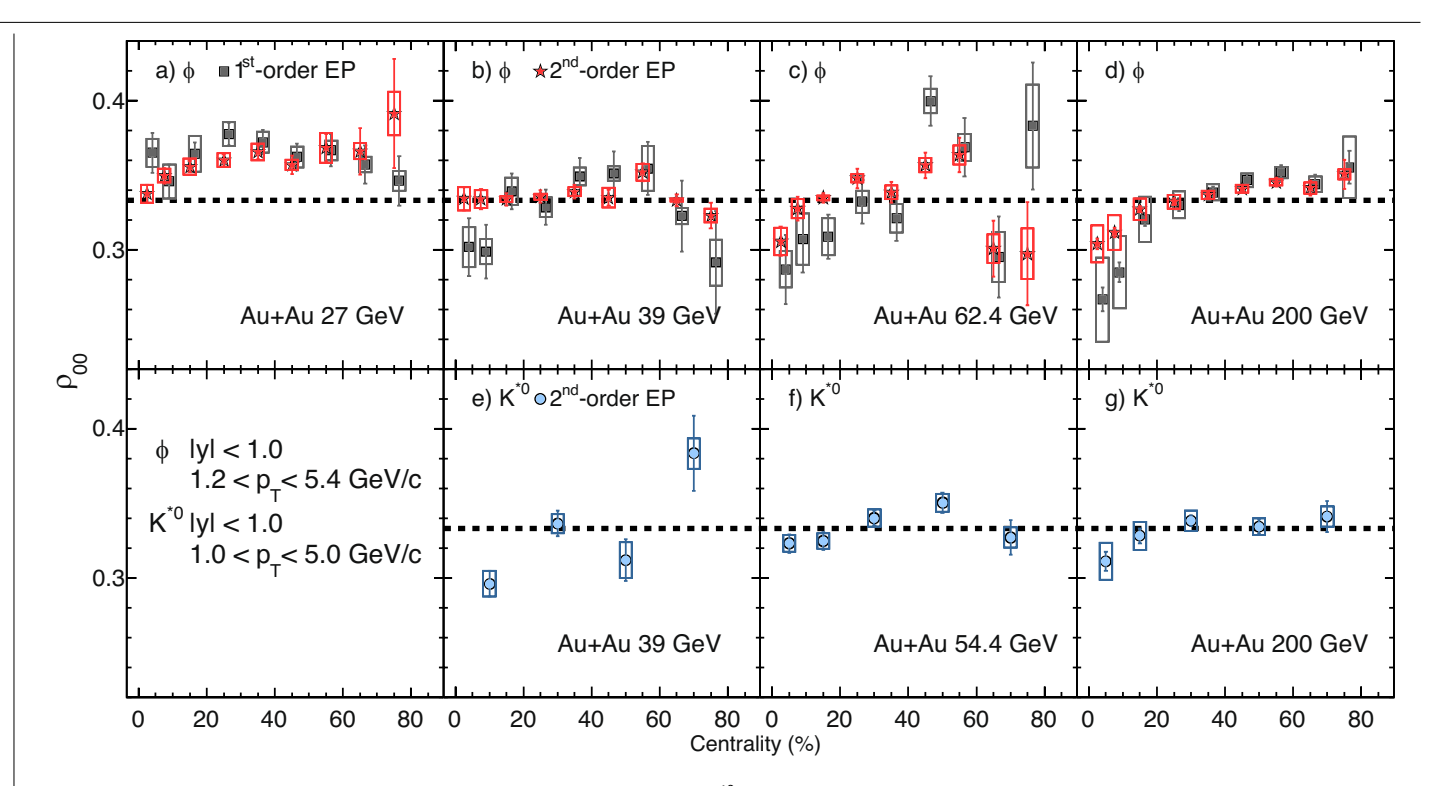
theoretical calculations with a  $\phi$ -meson field<sup>2</sup>. The corresponding  $G_s$  values obtained from the fits are shown in the legend.



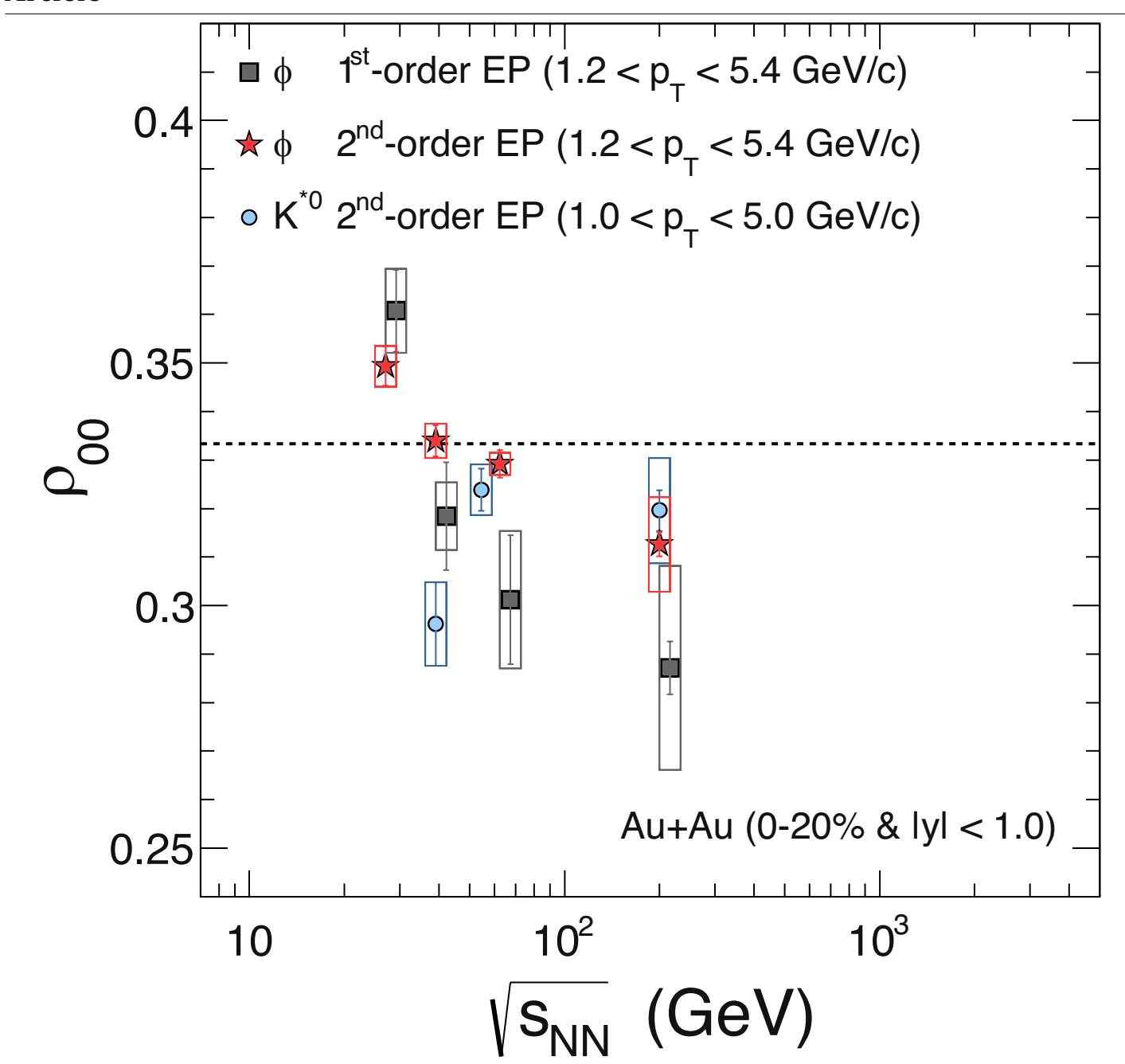
Extended Data Fig. 6 |  $\rho_{00}$  as a function of transverse momentum for  $\phi$  for different collision energies. The grey squares and red stars are results obtained with the first-order and second-order event planes, respectively.



**Extended Data Fig. 7** |  $\rho_{00}$  **as a function of transverse momentum for K\*0 for different collision energies.** The solid circles are results obtained with the second-order event plane.



**Extended Data Fig. 8**  $|p_{00}|$  as a function of centrality for  $\phi$  (upper panels) and  $K^{*0}$  (lower panels). The solid squares and stars are results for the  $\phi$  meson, obtained with the first-order and second-order event planes, respectively. The solid circles are results for the  $K^{*0}$  meson, obtained with the second-order event plane.



Extended Data Fig. 9 | Global spin alignment measurement of  $\varphi$  and  $K^{*0}$  vector mesons in Au+Au collisions at 0–20% centrality. The solid squares and stars are results for the  $\varphi$  meson, obtained with the first-order and second-

order event planes, respectively. The solid circles are results for the  $K^{*0}$  meson, obtained with the second-order event plane.

### Extended Data Table 1 | Sources of systematic error in $\boldsymbol{\varphi}$

	Quality Cuts	PID Cuts	Signal & Yields Extraction	Efficiency	Total
1st-order EP	0.0015	0.0017	0.0031	0.0017	0.0042
2nd-order EP	0.0006	0.0006	0.0013	0.0005	0.0017

The tabulated numbers are absolute uncertainties in  $\rho_{00}$ .

## Extended Data Table 2 | Sources of systematic error in K\*0

	Quality Cuts	PID Cuts	Signal Extraction	Yields Extraction	Total
2nd-order EP	0.0018	0.0020	0.0030	0.0015	0.0043

The tabulated numbers are absolute uncertainties in  $\rho_{00}$ .